CHAPTER 17

Sputtering and Laser Ablation

Herbert M. URBASSEK

Fachbereich Physik
Universität Kaiserslautern
Erwin-Schrödinger-Straße
D-67663 *Kaiserslautern*, *Germany*
E-mail: *urbassek@rhrk.uni-kl.de*
url: *http://www.physik.uni-kl.de/urbassek/*

DOI: 10.1016/S1573-4331(08)00017-6

Handbook of Surface Science
Volume 3, edited by E. Hasselbrink and B.I. Lundqvist

Contents

Abstract

The physical mechanisms and processes underlying the erosion of a surface induced by ion bombardment or short-pulse laser irradiation are presented. The stopping of the ion, its energy deposition in the electronic and atomic system and the build-up of a linear collision cascade are reviewed. Linear sputtering occurs when recoiling target atoms can surpass the surface barrier. When the average energy delivered per atom in the vicinity of the surface becomes comparable to the cohesive energy of the solid, sputtering from a so-called spike may result. This scenario is particularly pronounced in the case of cluster impact. The materials phenomena occurring after ultra-fast laser irradiation of a metal in the ps- or fs-regime are highlighted, and the thermomechanical spallation process is characterized in detail.

This page intentionally left blank

17.1. Introduction

In this chapter, the physics underlying the erosion of solids by ion impact or laser irradiation will be presented. While differing in many aspects, these two forms of irradiation deliver such a high amount of energy to the surface of the irradiated material that it is sufficient for bond breaking and hence induces surface erosion. Furthermore, in contrast to temperature-induced evaporation, the processes occur out of equilibrium since, as a consequence of the sudden perturbation induced by the irradiation, erosion occurs fast. Both these aspects, and in particular their non-equilibrium nature, make the processes occurring under energetic ion bombardment or intense laser irradiation a fascinating subject also for fundamental interest.

In this presentation, I will restrict attention to the case of elemental targets, thus avoiding the complications arising as a consequence of the bombardment-induced concentration changes in compound targets. Furthermore, in the case of laser irradiation, I will concentrate on (ultra-) short pulse irradiation, i.e., pulse durations in the regime of several ps and below. It is exactly in this range of short pulses, where analogies between the erosion behavior due to ion and laser irradiation are most pronounced, cf. Fig. 17.1.

17.2. Sputtering by ion bombardment

17.2.1. Stopping

The projectile ion delivers its energy in a series of collisions to the target atoms, and also to the target electronic system. These two channels of energy loss have been termed *elastic* and *inelastic*, respectively. Lindhard et al. (1968) introduced the approximation that these two energy loss channels can be treated independently, such that the total energy loss is given by the sum of these two contributions. In the following, we shall first discuss the physics underlying elastic collisions.

17.2.1.1. Potentials

The interaction potential between a projectile and a target atom, and also between two target atoms, has the following generic form:

(i) At small distances, the interaction is purely repulsive, due to the electrostatic repulsion of the nuclei and of the inner electron shells, but also – towards lower interaction energies – due to the so-called Pauli repulsion. The latter denotes an increase of the potential energy of two atoms with overlapping electron shells, where the Pauli principle promotes electrons to higher energy states.

(ii) At larger separation, the interaction potential is attractive due a covalent, ionic or metallic chemical bonding or due to van-der-Waals interactions. In this attractive regime, the potential energy is generally of a many-body nature, i.e., the attraction between two atoms depends on the number and positions of the surrounding neighbor atoms. This attractive force is considered not to be of importance for particle stopping. It however influences sputtering both directly, since it is responsible

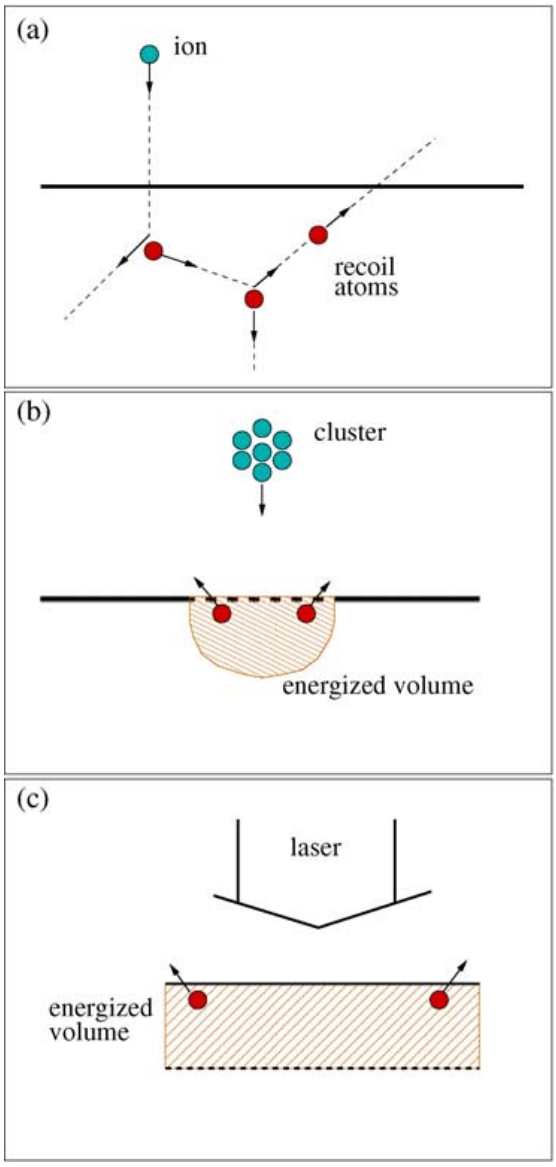

Fig. 17.1. Schematical survey of the sputtering and ablation regimes covered in this review: (a) collision-cascade or linear sputtering induced by ion impact; (b) sputtering from a so-called spike, which might be induced by cluster impact; (c) laser ablation. The shaded areas denote regions of high energy density.

for the surface binding energy, which sputtered particles have to overcome (Section 17.2.3), and indirectly, since it governs phase changes (melting, phase explosion, gasification), which are the mechanisms for spike sputtering (Section 17.3).

The repulsive part of the potential is usually well described as a pair potential between the energetic projectile and a low-energy target atom, since the surrounding neighbors are too distant to influence this close collision. Due to their relevance for particle stopping, the two-atom repulsive potentials have been calculated repeatedly in the past. This has been done using either methods from quantum chemistry or from density functional theory. In principle, and also in practice, stopping calculations can be based on the individual

projectile-target-atom system of interest. However, often it has been found useful to invoke scaling properties, which are based on the Thomas–Fermi theory of the atom. These scaling relations, while being accurate only up to several percent for individual systems, allow to analyze the stopping behavior in more general terms.

Consider the collision of two atoms with nuclear charges Z_1 and Z_2 and masses M_1 and M_2. In the repulsive regime, the binary interaction potential $V(r)$ may be written as

$$V(r) = \frac{Z_1 Z_2 e^2}{r} \Phi\left(\frac{r}{a}\right), \tag{17.1}$$

where Gaussian units have been adopted, i.e., $e^2 = 14.40$ eV Å. The screening function Φ introduces a length scale, the so-called screening radius a. In the original formulation of Lindhard et al. (1968), which was based on similarity considerations within the Thomas–Fermi theory of the atom, the screening length is given by

$$a_{\mathrm{TF}} = 0.885 a_0 \left(Z_1^{2/3} + Z_2^{2/3}\right)^{-1/2}, \tag{17.2}$$

where a_0 is the Bohr radius. In the often employed so-called ZBL potential developed by Ziegler et al. (1985), a different screening length has been adopted on purely empirical grounds:

$$a_{\mathrm{ZBL}} = 0.8853 a_0 \left(Z_1^{0.23} + Z_2^{0.23}\right)^{-1}. \tag{17.3}$$

The ZBL potential is employed in the widespread TRIM (Eckstein and Biersack, 1984) and SRIM (Ziegler, 2000, 2004) program codes, which calculate particle stopping, energy deposition, ranges, and sputtering on the basis of a Monte Carlo algorithm.

The screening function Φ is parameterized as a sum of exponentials

$$\Phi(x) = \sum_{i=1}^{n} c_i e^{-d_i x}, \tag{17.4}$$

where c_i and d_i are constants and n assumes values up to $n = 3$ or 4. For the ZBL potential, it is $n = 4$ and

$$\begin{aligned} \Phi_{\mathrm{ZBL}}(x) = {} & 0.1818 e^{-3.2x} + 0.5099 e^{-0.9423x} + 0.2802 e^{-0.4029x} \\ & + 0.02817 e^{-0.2016x}. \end{aligned} \tag{17.5}$$

We plot in Fig. 17.2 the potential between an Ar and a Au atom as calculated using density functional theory and compare to the ZBL potential. Figure 17.2 exemplifies that the repulsive binary interaction is at higher energies reasonably well described by using available parameterizations, such as the ZBL potential, while the latter becomes too repulsive at smaller energies (Karolewski, 2006).

Since a single length scale, a, governs the potential equation (17.1), the so-called Thomas–Fermi (or Lindhard) energy

$$E_L = Z_1 Z_2 e^2 / a_{\mathrm{TF}} \tag{17.6}$$

gives a convenient energy scale. For example, the Lindhard energy amounts to $E_L = 220$ keV for Ar $\rightarrow$ Au and 1.16 MeV for Au $\rightarrow$ Au collisions. It allows to introduce

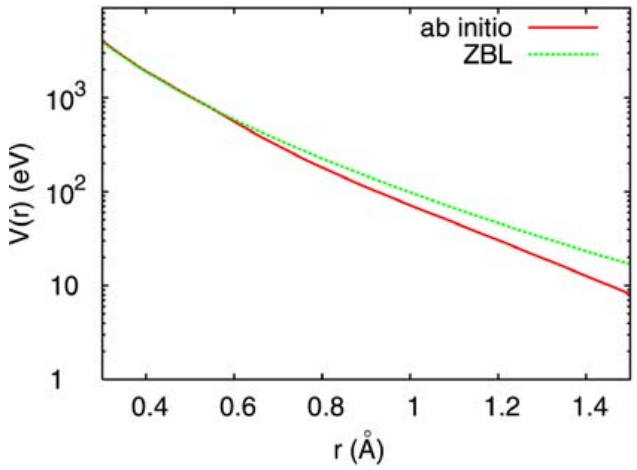

Fig. 17.2. Potential $V(r)$ describing the interaction between an Ar and a Au atom at short distances, $r < 1.5$ Å. Ab-initio data calculated by density functional theory (Karolewski, 2006). The agreement with the often employed so-called ZBL potential is reasonably good, in particular for higher energies.

a *reduced* energy as

$$\epsilon = \frac{E_{\rm rel}}{E_L} = \frac{a_{\rm TF} E_{\rm rel}}{Z_1 Z_2 e^2}, \tag{17.7}$$

where $E_{\rm rel}$ is the relative interaction energy between the two collision partners. It is $E_{\rm rel} = M_2 E/(M_1 + M_2)$ for an atom of mass M_1 and energy E hitting an atom of mass M_2 at rest.

For qualitative orientation it proves often useful to approximate the potential by a power law

$$V(r) = K r^{-1/m}, \tag{17.8}$$

where the exponent m may have a value between 0 and 1. For a fixed value of m this is obviously possible only over a restricted range of energies. For very high energies $\epsilon \gg 1$, $m = 1$ is valid. For $0.1 \lesssim \epsilon \lesssim 2$, $m = 1/2$ has been advocated. For $\epsilon \lesssim 10^{-3}$, a value of m with $0 \leqslant m \lesssim 1/4$ should be characteristic.

17.2.1.2. Cross sections

When describing the collisions of two atoms, one is often not interested in the details of the trajectory, but rather in the statistics of energy transfer. This is conveniently given by the *cross section*. It may be defined as follows: If a particle of energy E moves a small distance ΔR in a random medium of atomic number density N consisting of particles at rest, the probability $\mathrm{d}P$ of undergoing a collision with energy transfer between T and $T + \mathrm{d}T$ is

$$\mathrm{d}P = N \Delta R \sigma(E, T)\, \mathrm{d}T. \tag{17.9}$$

The cross section σ can be calculated from the potential V by well known rules (Landau and Lifshits, 1960). For power potentials, Eq. (17.8), it is straightforward to show by a

scaling argument (Landau and Lifshits, 1960; Lindhard et al., 1968) that

$$\sigma(E, T)\,\mathrm{d}T = C_m E^{-2m} g\left(\frac{T}{E}\right)\frac{\mathrm{d}T}{E}, \tag{17.10}$$

with a constant C_m and a dimensionless function g. Lindhard et al. (1968) recommend the approximation $g(t) = t^{-1-m}$, such that

$$\sigma(E, T)\,\mathrm{d}T = C_m E^{-m} T^{-1-m}\,\mathrm{d}T. \tag{17.11}$$

The cross section constant C_m is given in terms of the masses and the atomic charges of the colliding atoms as

$$C_m = \frac{\pi}{2}\lambda_m a^2\left(\frac{M_1}{M_2}\right)^m\left(\frac{2Z_1 Z_2 e^2}{a}\right)^{2m}, \tag{17.12}$$

where λ_m is a dimensionless number depending on the cross section exponent m, tabulated by Sigmund (1981); cf. also Vicanek et al. (1989).

17.2.1.3. Stopping power

An important information to be obtained from the cross section is the average energy loss ΔE a particle of energy E suffers when travelling a path length ΔR. With the probability $\mathrm{d}P$ of Eq. (17.9) it is

$$\Delta E = \int T\,\mathrm{d}P = N\Delta R\int T\sigma(E, T)\,\mathrm{d}T. \tag{17.13}$$

For infinitesimal ΔR, this leads to the concept of the (nuclear) *stopping power*

$$\frac{\mathrm{d}E}{\mathrm{d}R} = -N S_n(E), \tag{17.14}$$

with the stopping cross section

$$S_n(E) = \int T\sigma(E, T)\,\mathrm{d}T. \tag{17.15}$$

For power law cross sections, Eq. (17.11), it is

$$S_n(E) = \frac{1}{1-m}C_m E^{1-2m} \tag{17.16}$$

for $M_1 = M_2$. Hence, for a hard interaction $m = 0$, the stopping power increases linearly with E, whereas for $m = 1/2$, i.e. around the maximum of the stopping power, it is constant.

For potentials (17.1) a dimensionless stopping power $s_n(\epsilon)$ can be introduced which is related to $S_n(E)$ by

$$S_n(E) = 4\pi a Z_1 Z_2 e^2\frac{M_1}{M_1 + M_2}s_n(\epsilon). \tag{17.17}$$

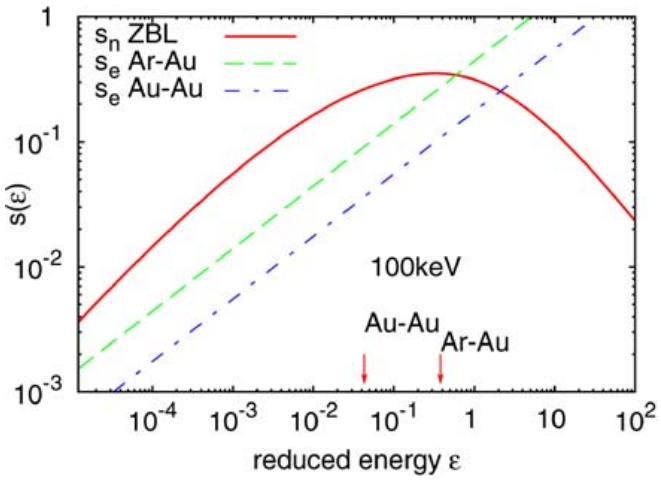

Fig. 17.3. Reduced nuclear and electronic stopping cross sections, $s_n(\epsilon)$ and $s_e(\epsilon)$, as a function of the reduced energy ϵ. The nuclear stopping has been calculated for the ZBL potential, Eq. (17.18), and the electronic stopping using the Lindhard–Scharff formula, Eq. (17.21), for the cases Ar $\rightarrow$ Au and Au $\rightarrow$ Au. The reduced energies for 100 keV projectiles have been indicated.

For the ZBL potential, the reduced stopping power can be approximated by (Ziegler et al., 1985)

$$s_n(\epsilon) = \begin{cases} \frac{\ln(1+1.1383\epsilon)}{2(\epsilon+0.01321\epsilon^{0.21226}+0.19593\epsilon^{0.5})}, & \epsilon \leqslant 30, \\ (\ln\epsilon)/(2\epsilon), & \epsilon > 30. \end{cases} \tag{17.18}$$

Figure 17.3 illustrates this function; for convenience, the reduced energies ϵ for a 100 keV Ar $\rightarrow$ Au and a 100 keV Au $\rightarrow$ Au collision have also been indicated. From Fig. 17.3 we observe three features:

(i) The stopping has a broad maximum for $0.1 < \epsilon < 1$. Here the maximum stopping power is $s_n = 0.35$ at $\epsilon = 0.33$. This amounts to $\mathrm{d}E/\mathrm{d}x = 90$ eV/Å for Ar $\rightarrow$ Au collisions at 80 keV and 1.0 keV/Å for Au $\rightarrow$ Au collisions at 700 keV.

(ii) Towards smaller energies, the stopping power decays towards 0 like ϵ^{1-2m}, cf. Eq. (17.16). The ZBL stopping power, Eq. (17.18), corresponds to $m = 0.11$. Note that a linear stopping power, $S_n \propto E$, is predicted for $m = 0$ and for a steep repulsive potential, i.e., hard spheres.

(iii) Towards high energies $\epsilon \gg 1$, the stopping power falls off like $(\ln\epsilon)/\epsilon$. This is characteristic of Coulomb scattering, where cross sections decay $\propto 1/E^2$ for large energies.

17.2.1.4. Electronic stopping

The energy transfer of an energetic ion to the target electrons, or to the solid target as a whole, is still a subject of intense research. In particular for slow ions, with energies <10 keV, say, experiments are not easily performed, since their realization with ultrathin foils is challenging, and furthermore, since nuclear stopping is the dominant energy loss mechanism for these small energies. On theoretical grounds, it is thought that for small

projectile velocities,

$$v < v_0 {Z_1}^{2/3}, \tag{17.19}$$

the projectile energy loss to electrons is proportional to the projectile velocity v, and hence resembles a friction process. Here $v_0 = e^2/\hbar = 2.2{\cdot}10^6$ m/s is the Bohr velocity. Lindhard and Scharff (1961) predict

$$S_e = 8\pi e^2 a_0 \frac{Z_1 Z_2}{Z} \frac{v}{v_0} {Z_1}^{1/6}, \tag{17.20}$$

where $Z = ({Z_1}^{2/3} + {Z_2}^{2/3})^{3/2}$. In reduced units this reads

$$s_e(\epsilon) = k\sqrt{\epsilon} \tag{17.21}$$

with a constant k

$$k = \frac{{Z_1}^{2/3} {Z_2}^{1/2}}{12.6 Z^{1/2}} \frac{(M_1 + M_2)^{3/2}}{{M_1}^{3/2} {M_2}^{1/2}}, \tag{17.22}$$

which assumes values in the range $k = 0.1-0.4$, except for very light ions on heavy targets. Thus, it is $k = 0.44$ for Ar $\rightarrow$ Au collisions and $k = 0.18$ for Au $\rightarrow$ Au collisions. In Fig. 17.3 we introduced the electronic stopping powers calculated for the Ar $\rightarrow$ Au and Au $\rightarrow$ Au systems and compare them to the nuclear stopping. It is seen that at small energies (below the maximum of the nuclear stopping power), electronic stopping can be neglected to a first approximation; this is typical of all bombardment cases with the exception of very light ions like H or He. Secondly, beyond the nuclear stopping power maximum, electronic stopping will dominate. These high energies, however, will not be of interest in the present contribution.

17.2.2. Implantation of the ion and damage in the target

17.2.2.1. Ranges

Due to nuclear and electronic stopping, the ion continuously loses energy until it is stopped. Its end position is called the *range* of the ion in the target. Due to the stochastic nature of the energy loss processes, also the range is a stochastic quantity, and is described by the range distribution $R(z)$; this is defined such that $R(z)\,\mathrm{d}z$ gives the probability that the projectile is stopped at a depth between z and $z + \mathrm{d}z$ inside the target. This quantity is of essential interest for the question of ion implantations, and has been thoroughly studied. Its calculation is a straightforward task that is nowadays mainly accomplished using Monte Carlo simulation methods.

Figure 17.4 gives an example of the range distribution calculated by the Monte Carlo code SRIM Ziegler (2000) for 10 keV Ar atoms incident on a Au target.

An analytical estimate of the range can be obtained as follows. Let us consider an ion of energy E_0 slowing down in a medium with dominantly nuclear stopping, $S_n(E_0)$. From Eq. (17.14) we obtain an approximation to the mean path length $R(E_0)$ of the projectile, measured along its zig-zag way in the solid:

$$R(E_0) = \int_0^{E_0} \frac{\mathrm{d}E}{NS(E)}. \tag{17.23}$$

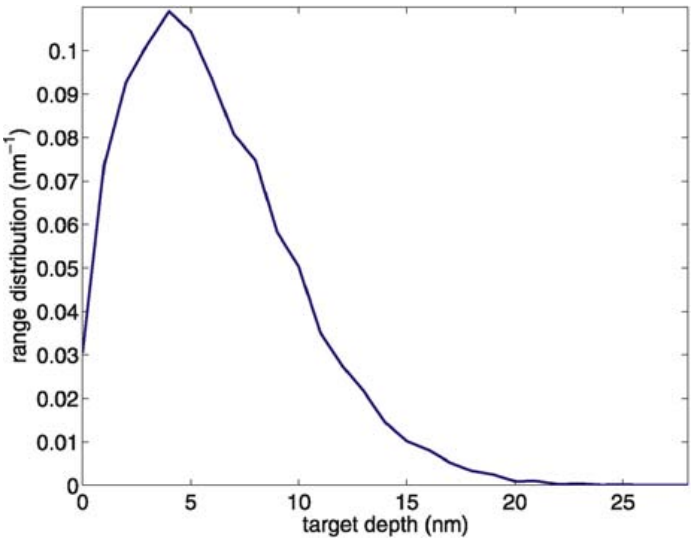

Fig. 17.4. Range distribution of 10 keV Ar atoms bombarding a Au target. Data obtained by a SRIM (Ziegler, 2000) calculation.

The *mean projected range* $R_p(E_0, \theta_0)$ of an ion impinging at an angle of incidence θ_0 on a target measures the distance from the surface to the end point of the projectile; it is shorter than $R(E_0)$ by a geometrical factor $\cos\theta_0$ and by a factor $f < 1$ which is only slowly dependent on energy:

$$R_p(E_0, \theta_0) = f \cos\theta_0 R(E_0). \tag{17.24}$$

For power cross sections, according to Eq. (17.15), R and hence R_p scale with energy as

$$R_p(E_0, \theta_0) \propto \frac{E_0^{2m}}{NC_m} \cos\theta_0. \tag{17.25}$$

17.2.2.2. Recoil generation: The linear cascade

While the projectile is slowed down, in each collision with a target atom, this target atom receives energy and recoils from its original position. Thus, after each collision, there is one more particle set in motion, which is slowed down in its term by elastic collisions and electronic stopping. This process of recoil generation keeps repeating.

In this way a collision cascade is set up. In the approximation that each recoil slows down in a target which is unaffected by the other recoils, this cascade has a self-similar structure (Winterbon et al., 1987). Due to the stochastic nature of particle slowing down and scattering, each individual collision cascade will look different from another. For most considerations, however, only the average properties of the cascade will be of interest.

Figure 17.5 exemplifies such a linear collision cascade by displaying the high-energy recoils ($E > 25$ eV) of a 10 keV Ar $\rightarrow$ Au cascade.

Two properties of the cascade are of particular interest for sputtering. These are the spatial structure of the cascade (Section 17.2.2.3), and the energetic structure of the cascade, in particular the question with which energies the recoils are created (Section 17.2.2.4).

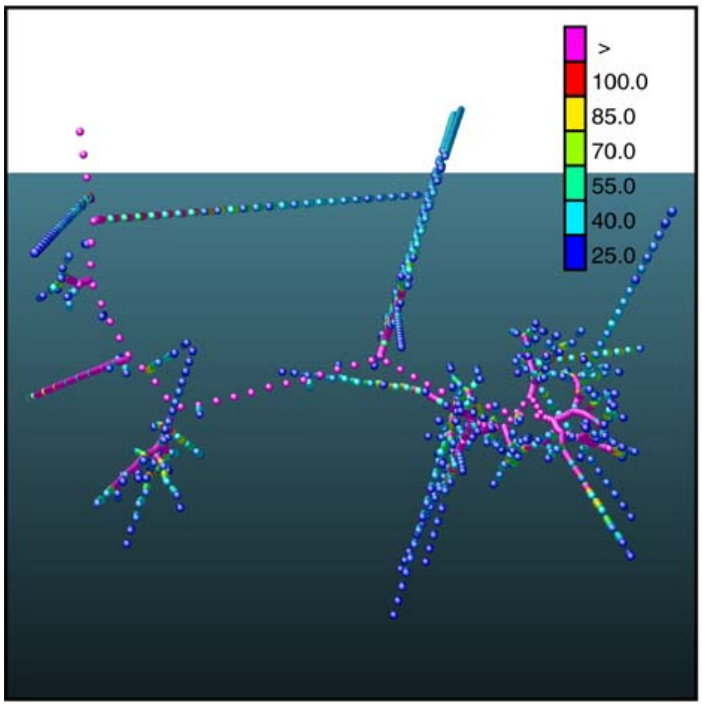

Fig. 17.5. Structure of a collision cascade as calculated by a molecular-dynamics simulation. The lateral size of the picture is about 20 nm. The projectile Ar atom enters a Au (111) crystal with 10 keV energy and an angle of 7° towards the surface normal. Only atoms which receive a kinetic energy above 25 eV (see scale at the upper right) are displayed. After a time of about 0.5 ps, the ion and all target atoms have an energy below the threshold, and the trajectories appear to end. Two atoms are sputtered as a dimer.

17.2.2.3. Deposited energy

The so-called *deposited-energy* distribution $F_D(z)\,\mathrm{d}z$ is defined as the amount of energy deposited in low-energy recoil motion in the target between depth z and $z + \mathrm{d}z$. This distribution gives the gross shape of the defect distribution in a cascade and is thus of considerable interest to the study of ion-induced damage and in particular point defects like vacancies and interstitials. The energy density at the surface, $F_D(z = 0)$, is decisive for calculating the sputter yield. The center position of the deposited-energy distribution follows a law similar to Eq. (17.25). The variance of the distribution in the direction perpendicular to the target surface and lateral to it can be taken to indicate the damage zone induced by a single projectile. Note, however, that this is an average over many individual collision-cascade shapes.

Figure 17.6 displays the deposited-energy distribution for the case of 10 keV Ar → Au, using the same SRIM calculation, with which the range distribution, Fig. 17.4, has been obtained.

17.2.2.4. Recoil spectrum and damage

Consider a cascade started by an ion of energy E_0. Let us denote by $F(E_0, E)\,\mathrm{d}E$ the average number of recoils with energy in the interval $(E, E + \mathrm{d}E)$. It can be shown that

$$F(E_0, E) = \Gamma_m \frac{E_0}{E^2} \tag{17.26}$$

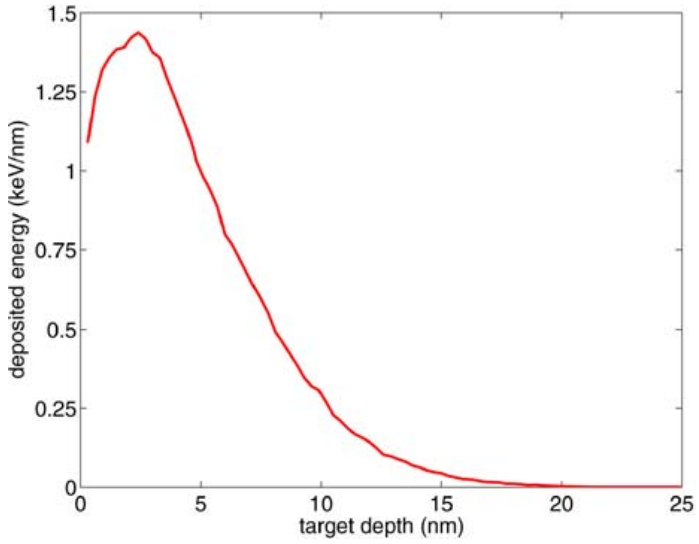

Fig. 17.6. Deposited-energy distribution $F_D(z)$ for the case of a 10 keV Ar atom bombarding a Au target. Data obtained by a SRIM (Ziegler, 2000) calculation.

with a number $\Gamma_m \cong 0.6$ only slightly depending on the potential exponent m. The total number of defects created in a collision cascade can be calculated from Eq. (17.26): Assume a displacement threshold E_d such that each recoil created with an energy above E_d leads to a stable Frenkel pair, while recoils generated with energies below E_d return to their initial lattice position, and no defect is formed. Then the number of defects (Frenkel pairs or vacancies) is given by

$$N_{\text{defects}} = 0.4\frac{E_0}{E_d}. \tag{17.27}$$

More refined estimates are available (Averback and Diaz de la Rubia, 1998).

It may be noted that the actual number of defects found after a single ion impact may lead to amorphization in semiconductors, whereas in metals the formation of a heat spike and the consecutive melting of the cascade core may anneal out part of the damage formed. An up-to-date report on ion-induced damage has been presented by Averback and Diaz de la Rubia (1998); for low-energy ion-induced damage, in particular in semiconductors, see also Gnaser (1999).

It is often of interest to determine the depth distribution of the damage formed. Thus, for studies of sputtering and sputter-induced surface changes, it may be relevant to know the amount of damage formed close to the surface. The deposited-energy distribution gives the gross shape of a cascade. However, in a cascade of course the interstitial and vacancy distributions will not coincide; the vacancies will lie rather more in the center of the cascade, while the interstitials will have been pushed out towards the periphery. In particular, the interstitial distribution will also be strongly determined by crystal effects, like replacement collision sequences.

17.2.3. Sputtering

A consequence of the energetic ion impact is the sputtering of the target, i.e., the emission of atoms, molecules or clusters from the target surface. In this section, we will consider the scenario of linear sputtering, or sputtering from a linear collision cascade, where particles are emitted from the surface due to momentum transfer from the projectile ion or a recoil in the collision cascade developing in the target. A different scenario, sputtering from dense cascades, will be considered in Section 17.3.

17.2.3.1. Sputter yields

In a sputter experiment, the quantity that is easiest to measure is the sputter yield Y. For an elementary target, it is defined as the average number of sputtered atoms per incident projectile. The yield depends on quite a few parameters of the projectile-target-system under consideration: on mass and atomic number of the projectile, and the target atom; on bombarding energy and direction; and on target material properties, in particular the surface binding that hinders atoms from leaving the surface. Nevertheless there exists a remarkably simple formula due to Sigmund (1969, 1972, 1981), which describes the sputter yield from collision cascades in a quantitative way. The formula reads

$$Y = \frac{1}{8} \frac{\Gamma_m F_D(z=0)\Delta x}{U}. \tag{17.28}$$

Here it is assumed that recoil atoms can only leave the surface, if their velocity component perpendicular to the surface is high enough to overcome a surface barrier of height U. Δx is a length characterizing the depth out of which recoils may be ejected. It is known by the name of depth of origin of sputtered atoms. With the exponent m describing the interaction potential of low-energy recoils, it reads

$$\Delta x = \frac{1}{1-2m} \frac{1}{NC_m} U^{2m}. \tag{17.29}$$

This is proportional to the range of a recoil of energy U, cf. Eq. (17.25).

Equation (17.28) has the following interpretation (Sigmund, 1969):

- $F_D(z=0)\Delta x$ is the amount of energy deposited near the surface that is available for sputtering.
- The number of recoils created with energy above U is $\Gamma_m F_D \Delta x / U$.
- The remaining factor $1/8$ accounts for the fraction of recoils that have the right direction to surpass the planar surface barrier.

The sputter yield formula (17.28) has been shown to describe the sputtering of elemental targets with a sufficient degree of accuracy when the assumptions on which it is based are fulfilled: Sputtering proceeds via a collision cascade mechanism, and the bombarding energy E_0 is high enough to guarantee the establishment of an isotropic, well developed cascade (Sigmund, 1987).

For dimensional reasons, the energy deposited near the surface must be proportional to the projectile stopping power

$$F_D(E_0, z=0) = \alpha N S_n(E_0), \tag{17.30}$$

where the proportionality factor α depends mainly on the ratio of target atom to projectile mass and the bombarding angle. For normal incidence and self-sputtering $\alpha \cong 0.25$, but it increases substantially for light projectiles, since these may easily be reflected back to the surface to deposit there more energy.

17.2.3.2. Threshold sputtering

Sputtering ceases when the energy of the impinging ion has dropped below a certain threshold energy, $E_{\rm th}$. From a large body of experimental and simulational data, Eckstein et al. (1993) found that the threshold energy depends on the surface binding energy U and on the mass ratio $\mu = M_2/M_1$ of the target atom mass M_2 to the projectile ion mass M_1 as

$$E_{\rm th}/U = 7.0\mu^{-0.54} + 0.15\mu^{1.12}. \tag{17.31}$$

At this threshold, sputtering sets in rather sharply. An empirical expression for the rise of sputtering at near-threshold energies has been given by Bohdansky (1984) as

$$Y_{\rm th}(E_0) = \left(\frac{1}{8}\frac{\Gamma_m F_D(z=0)\Delta x}{U}\right)\cdot \eta\left(\frac{E_{\rm th}}{E_0}\right), \tag{17.32}$$

where the first term in brackets on the right is the sputter yield of Eq. (17.28) and $\eta(x)$ denotes the threshold function

$$\eta(x) = \left(1 - x^{2/3}\right)(1-x)^2 \quad (0 < x < 1). \tag{17.33}$$

In the near-threshold regime, the collision cascade is not yet fully established. Since only few collisions occur and the number of recoils is small, this regime has been called the *single-knock-on regime* (Sigmund, 1981).

Recently, Wittmaack (2003) has compiled the available experimental data base of sputtering of a Si target; the data are displayed in Fig. 17.7a. Impact energies vary over more than three decades, and both light and heavy projectiles have been included. Wittmaack showed that this data set can be well described by the theory presented here, cf. Fig. 17.7b: To this end, observe that the energy dependence of the sputter yield Y, Eq. (17.28) is only given by the stopping power, $Y = C \cdot s_n(\epsilon)$, where C contains all remaining (energy-independent) factors of Eq. (17.28). Introducing therefore a *reduced sputter yield* as

$$y = \frac{Y}{C}, \tag{17.34}$$

the above analysis shows that all experimental sputter data should align on a single line

$$\frac{y}{\eta} = s_n(\epsilon). \tag{17.35}$$

As Fig. 17.7b shows, the agreement between experiment and theory is more than satisfactory. It should be noted that Wittmaack (2003) employed the KrC stopping power as given by Garcia-Rosales et al. (1994) rather than the ZBL stopping power, Eq. (17.18).

17.2.3.3. Surface binding energy

The surface binding energy U is generally set equal to the cohesive energy (sublimation energy) of the solid. This is justified for an atomically rough surface, as it is created after

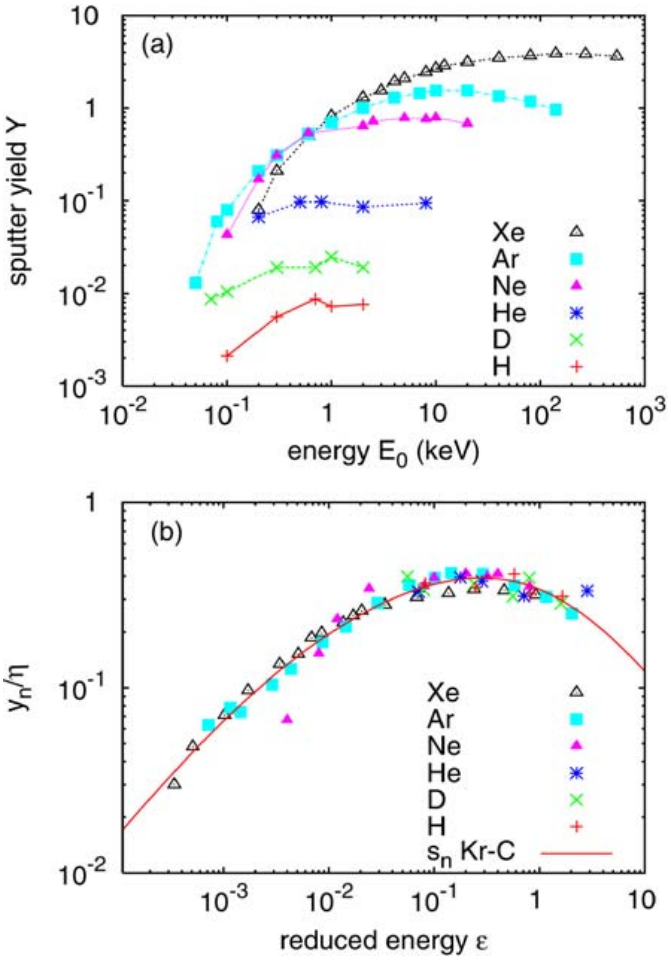

Fig. 17.7. (a) Compilation of experimentally determined sputter yields of Si with normally incident ions. Data taken from Wittmaack (2003). Lines are to guide the eye. (b) Reduced sputter yields, Eq. (17.34), align well with the reduced nuclear stopping cross section. Analysis due to Wittmaack (2003).

prolonged sputtering: then, each surface atom will be bound on average with half the number of bonds that it has in the bulk. In fact, when several layers have been sputtered away, the cohesive energy has to be invested per atom for the atomization of these layers. This argument also shows that the surface binding energy of an atom in a dense crystal surface plane should be higher than the cohesive energy, since every atom will have a relatively high number of neighbors. For the case that bonding is better described by a many-body interaction, such as is adequate for metals, this argument was extended to give a quantitative description of the crystallinity dependence of the surface binding energy (Gades and Urbassek, 1992, 1994b).

17.2.3.4. Sputtered atom energy distribution

In a sputter experiment the *flux* $f(E)$ of atoms out of the target surface is measured. This must be related to the recoil density at the target surface $z = 0$ (Falcone and Sigmund, 1981). To this purpose, the space dependence can be included in the recoil density by

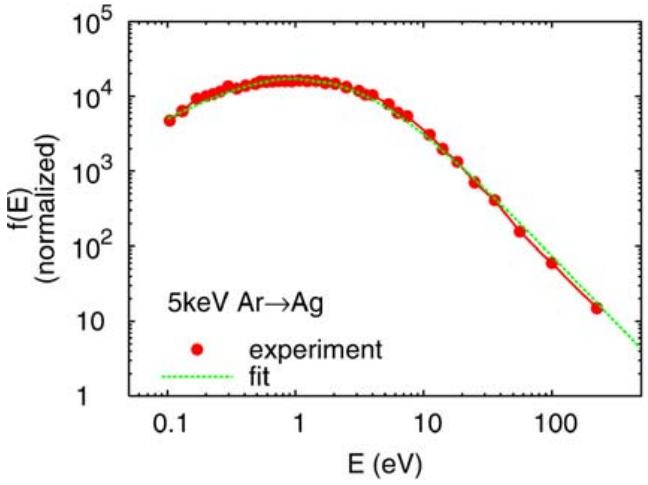

Fig. 17.8. Kinetic energy distribution of neutral Ag atoms sputtered from a polycrystalline Ag sample by bombardment with 5 keV Ar ions at 45° impact angle. Fit to Eq. (17.38) with surface binding energy $U = 2.94$ eV and power exponent $m = 0.15$. Data taken from Wahl and Wucher (1994).

replacing E_0 in Eq. (17.26) by F_D:

$$F(E, z) = \frac{\Gamma_m F_D(z)}{E^2}. \tag{17.36}$$

Hence the sputter flux can be obtained as

$$f(E)\,\mathrm{d}E \propto F(E, z = 0)\,\mathrm{d}E\Delta x \propto \frac{F_D(z = 0)}{E^2} E^{2m}\,\mathrm{d}E. \tag{17.37}$$

Obviously, for a hard interaction ($m = 0$), the sputtered flux follows an E^{-2}-law. For an interaction characterized by $m > 0$ it changes to a softer decay, due to the fact that higher-energy particles may originate from larger depths to contribute to the flux.

In order to escape from the surface, particles have to overcome a surface barrier. Usually a planar barrier is assumed, which acts only on the velocity component of the particle perpendicular to the surface, leaving the parallel velocity component unchanged. When one assumes the flux to be cosine-distributed in angle, a planar barrier of height U changes the flux (17.37) to

$$f(E) \propto \frac{E}{(E + U)^{3-2m}}. \tag{17.38}$$

For $m = 0$ this equation is known as Thompson's formula (1968). For $m \cong 0$, it well describes measured energy distributions of sputtered atoms. Figure 17.8 gives an example of the excellent quality of the Thompson formula for a specific case.

17.2.3.5. Angular distribution

When an energetic projectile produces a recoil cascade in an *infinite medium* (i.e. one without a surface), high-generation recoils will have forgotten the initial direction of the projectile and the cascade becomes *isotropic*. Hence the particle flux through an imaginary surface is cosine-distributed.

For sufficiently high energy bombardment, $E_0 \gtrsim 10$ keV, say, measured sputtered particle angular distributions however tend to become overcosine, i.e. there is an excess of particles sputtered in the direction perpendicular to the surface (Andersen et al., 1985). This may be rationalized as the influence of the target surface: Since the surface acts as a drain on target recoils, near to the surface recoils move preferentially towards the surface, rather than into the target. This establishes a cascade anisotropy that is present even for high-generation recoils and agrees with the experimentally measured overcosine distributions (Waldeer and Urbassek, 1987).

The angular distribution is however quite sensitive to the influence of target surface roughness and topography (Littmark and Hofer, 1978) and to target crystallinity. It changes furthermore if the target does not have a homogeneous composition in the first surface layers (Sigmund et al., 1982). This may be the case in nonelemental targets, after high implantation doses, or when adsorption layers form on the target surface.

17.2.3.6. Depth of origin

The depth from which sputtered atoms originate is relevant for assessing the depth resolution of sputtering-based depth-profiling methods. Since for low-energy recoils, $m = 0$, Eq. (17.29) gives the average depth of origin as

$$\Delta x = 1/NC_0. \tag{17.39}$$

With the original value of the low-energy stopping cross section C_0, this resulted in 5 Å (Sigmund, 1969). However, this value has been recalculated by Vicanek et al. (1989) who found that C_0 should be increased by a factor of 2, thus resulting in a depth of origin of $\Delta x = 2.5$ Å. Recent computer simulations (Glazov et al., 1998; Shulga and Eckstein, 1998) demonstrated that the escape depth is a factor of 4 smaller than the original estimate by Sigmund (1969). This is in reasonable agreement with experimental data by Wittmaack (1997, 2003), who showed particles to be mainly sputtered from the topmost surface layer. We note that the computer simulations of Shulga and Eckstein (1998) predict a dependence on the atomic number density proportional to $N^{-0.86}$ instead of N^{-1} as in Eq. (17.39).

The depth of origin of a sputtered particle can be expected to be slightly dependent on its energy E. In analogy to Eq. (17.29), we obtain

$$\Delta x = \frac{1}{1-2m}\frac{E^{2m}}{NC_m}. \tag{17.40}$$

This means that it can be expected that higher-energy sputtered particles originate from greater depths. This expectation is corroborated by computer simulation (Biersack and Eckstein, 1984; Shulga and Eckstein, 1998). Molecular-dynamics simulations typically show that for low impact energies, all sputtered atoms originate from the first target layer (Betz et al., 1994). With increasing energy, also deeper-lying atoms start to be emitted.

17.2.3.7. Fluctuations in sputtering

Even for a well defined target surface and well defined ion bombardment energy and angle, the collision cascade and the sputtering induced may fluctuate strongly between individual ion impacts. This is a consequence of the stochastic nature of the projectile slowing down and recoil generation. In fact, consider the extreme cases of the ion hitting

head-on centrally on a surface atom, or on the other hand hitting the surface in the middle of an open channel. In the first case, the collision cascade will develop close to the surface and induce strong sputtering; in the latter case, it may lead to only moderate recoil generation in the vicinity of the surface and hence little sputtering. In many experiments, only the average over a large number of individual ion impacts is measured, and hence fluctuations are of minor relevance. However, the surface topographical features evolving around each individual impact point will also fluctuate along with the energy deposition close to the surface and the sputter yield, and hence all sputter experiments based on direct inspection of the surface changes induced by single ion impacts measure these fluctuations.

Mainly from computer simulation data, it has been found that the sputter yield distribution is broad. While details depend on the bombardment condition (Eckstein, 1988), as a general rule of thumb it is found that the standard deviation of the sputter yield distribution is of the same order of magnitude as the average sputter yield (Conrad and Urbassek, 1990). An issue of particular interest is the fact that – albeit with a small frequency – high-yield events may occur, in which the individual sputter yield is considerably larger than the average. This issue is important for explaining cluster sputtering data.

17.2.3.8. Surface topography changes

As the result of ion impact on the target, damage will be created not only in the bulk, but also at the surface. Atomic defects may be categorized as surface vacancies (missing atoms in the topmost target layer) and adatoms. Among extended defects one finds adatom and vacancy islands, and even craters. Surface topographical features are accessible to measurements by scanning tunnelling microscopy (Michely and Comsa, 1991; Michely and Krug, 2004). These yield valuable information on the surface-near features of the cascade and on the sputter process. Since the consequences of individual ion impact become visible, also information on the sputter statistics becomes accessible.

Linear cascade theory can predict the adatom yield Y_a, i.e., the average number of adatoms due to ion impact. Let us denote by U_a the energy necessary to form an adatom. For example, for the (111) surface of an fcc metal, it is $U_a \cong 0.4U$. The recoil energy spectrum, Eq. (17.26), can be used to calculate the adatom yield Y_a, with the result $Y_a/Y \cong 4$. This is in agreement with experimental (Michely and Teichert, 1994) and simulational (Gades and Urbassek, 1994a) results of rare-gas bombardment of a Pt (111) surface for energies above 100 eV.

17.2.3.9. Cluster emission

It is a common experience that besides monatomic particles, clusters are found in the sputtered particle flux. In fact, surprisingly large clusters can be emitted. As an example, in 15 keV Xe bombardment of a Ag sample, (neutral) Ag_n clusters up to $n \cong 60$ have been found (Staudt et al., 2000). In fact, emission of clusters containing more than 500 atoms has been observed by Rehn et al. (2001) for 500 keV rare-gas ion impact on Au (cf. also the molecular-dynamics simulation displayed in Fig. 17.9). Since clusters must originate from a single ion impact event, the fact that clusters larger than the average cluster yield are sputtered, points at the importance of sputter yield fluctuations. Observed mass distributions follow a polynomial decay with cluster size

$$Y_n \propto n^{-\delta}, \tag{17.41}$$

where Y_n denotes the yield of clusters containing n atoms; the exponent δ has been empirically found to be inversely correlated to the average sputter yield Y (Wahl and Wucher, 1994). Up to now, sputter theory has not come up with an intuitive quantitative argument to explain such a polynomial decay, even though a number of theoretical investigations into the nature of large-cluster emission have been performed, cf. Reimann (1993). However, from molecular-dynamics simulations, it appears that large-cluster emission requires the correlated ejection of a group of neighboring atoms from the surface (Betz and Husinsky, 1995). The simulation of particularly energetic events, where a high amount of energy is deposited close to the surface, shows that even quasi-hydrodynamic droplet emission (clusters containing more than 100 atoms) is possible in specific cases, cf. the discussion in Section 17.3.2 and Fig. 17.9.

Sputtered clusters are internally hot after emission (Urbassek and Hofer, 1993). As a rule, the larger clusters are found to be metastable and to evaporate off atoms to cool. This experimental finding is corroborated by molecular-dynamics simulations which find sputtered clusters to possess high internal energy (Wucher and Garrison, 1992a, 1992b).

Dimers are the most abundant cluster species sputtered. Originally it was thought that dimers form upon sputtering from an elemental target when two atoms are sputtered more or less independently and combine to form a cluster in the vicinity of the surface (so-called *recombination* or *double-collision* model) (Gerhard and Oechsner, 1975; Können et al., 1974, 1975). Such a model led to the prediction of a translational energy spectrum which decays at high energies like E^{-5}; an even higher fall-off was predicted for larger clusters. This prediction is not confirmed by experiment, where in particular the larger clusters show comparable high-energy decay laws, cf. e.g. Wahl and Wucher (1994). This must be taken as evidence that clusters do not originate from individual (independent) emission events.

17.3. High energy densities: Sputtering from spikes

The linear-cascade picture, where an energetic atom collides with target atoms at rest, which in their term recoil and collide with other target atoms at rest, etc., breaks down, when the majority of atoms in a certain volume have been set in motion. This is invariably the fate of every linear collision cascade at large times. However, often, this late stage is of little experimental consequence since the energy of the moving atoms has dropped too low. However, in cases of high energy density, a number of physical effects may be induced in this so-called spike stage.

As Sigmund (1974) notes, "Spike effects may be important when the spike life time is larger than the duration of the initiating cascade. Spikes have been considered as the origin of a variety of experimental results over the years. The more compelling evidence seems to come from sputtering experiments". The notion of a spike has been invoked in particular for the discussion of ion-induced damage since the work by Brinkman (1954) and Seitz and Köhler (1956). Various epithet have been introduced to qualify a spike either as a *displacement spike*, a *thermal spike*, or an *elastic collision spike*. We shall not be concerned with these differences here.

In a spike, thermal equilibrium can be established locally quite fast among the moving atoms. From gas-phase physics it is known that such an equilibrium will be established

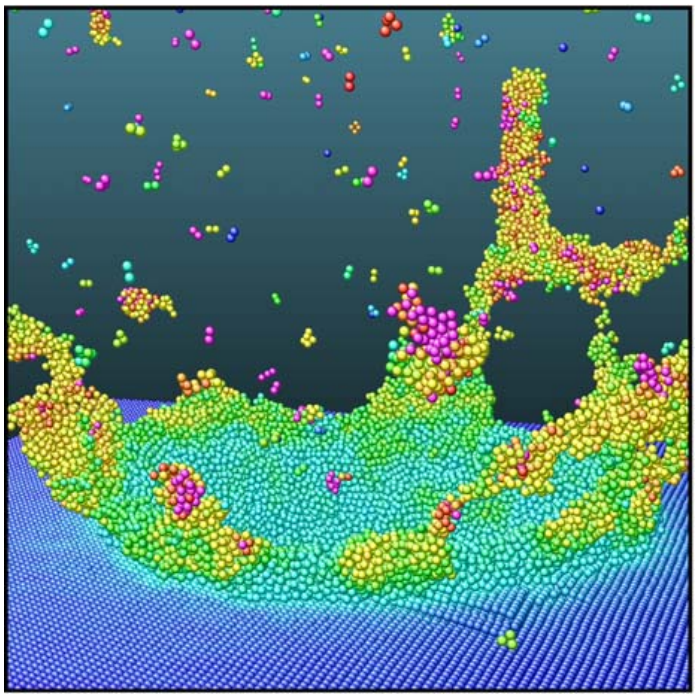

Fig. 17.9. Perspective view of a Au target bombarded by a Au_8 cluster with an energy of 16 keV/atom. The snapshot taken at 32 ps after cluster impact has been obtained by a molecular-dynamics simulation. The gray-shade (color online) illustrates the local temperature (i.e., the local kinetic energy averaged over a sphere of 6.2 Å radius in the center-of-mass frame). Color online: Blue: 0 K. Green: Molten (1338 K). Purple: Hotter than 2667 K.

when each atom has undergone a few (of the order of 3–10) collisions (Weller and Weller, 1982; Waldeer and Urbassek, 1991). In a solid, the time may accordingly be estimated to be $t_{\text{therm}} \cong (3\text{–}10)/\nu_D$, where ν_D is the Debye frequency. For instance, in the case of Au, which has a small Debye frequency, it is $\nu_D = 3.4$ THz, and thus after around 1–3 ps, thermal equilibrium will have been established locally. After this time it is possible to describe the state of matter using hydrodynamic and thermodynamic concepts like the density $n(\mathbf{r}, t)$ the temperature $T(\mathbf{r}, t)$ and the pressure $p(\mathbf{r}, t)$. These concepts allow to describe the behavior of the material after irradiation, and in particular the sputtering process, in a way which is different from the collision-cascade physics described above.

Figure 17.9 presents an atomistic view of the processes occurring in a Au target after impact of a Au_8 cluster with 128 keV total energy. It is clearly seen that the violent materials effects occurring cannot be described using the model of a linear-collision cascade. Rather, macroscopic concepts like temperature and boiling are appropriate for describing this process.

The spike concept has been used to describe the phenomena of defect formation and in particular defect annealing in the aftermath of a collision cascade, and it has been found that in metals the spike systematically tends to reduce the number of point defects formed due to the thermally activated annihilation processes occurring (Nastasi et al., 1996; Averback and Diaz de la Rubia, 1998). The concept of a spike has also been extensively used to describe ion-induced mixing and it has been found that mixing processes can be enhanced or reduced in the spike phase after the collision cascade (Cheng, 1990;

Nastasi et al., 1996; Süle et al., 2003). For ion-induced sputtering, spikes have been invoked to describe particularly large sputter yields and also strong surface-topographical features, in particular crater formation under ion impact (Andersen, 1993; Reimann, 1993). Quite generally, spike effects on sputtering can be assumed to be strong, when in a limited volume close to the target surface, the energy per atom E_0 is sizeable compared to the cohesive energy E_{coh} of the target; or, in other terms, when the local temperature T is sizeable when compared to the critical temperature T_c of the liquid-vapor phase transition.

17.3.1. Models

A number of models have been developed to describe sputtering from spikes. None of these appear to be able to describe quantitatively the variety of experimental results available. But each of them features a characteristic element important for the sputtering phenomena: Surface boiling, phase explosion, the importance of high pressures, etc. So several of the models available will be described briefly:

(i) *Surface evaporation*: Assume the energized region to be of cylindric form with the axis aligned with the ion impact direction; this will be in the case considered here directed perpendicular into the solid. When the initial lateral distribution of the deposited energy or 'temperature' is of Gaussian form with maximum T_0, sputtering can be described from the interplay of surface evaporation over the surface barrier U and lateral heat conduction. An evaluation of this idea gives (Johnson and Evatt, 1980; Sigmund and Claussen, 1981)

$$Y = g\left(\frac{kT_0}{U}\right) \cdot \left(\frac{\mathrm{d}E}{\mathrm{d}x}\right)^2 . \tag{17.42}$$

The function g depends on details of the model. In any case, $g(kT_0/U)$ approaches a constant for $kT_0 \gg U$. Thus, for a hot narrow spike the yield is quadratic in the stopping power $\mathrm{d}E/\mathrm{d}x$ – in contrast to the linear dependence of Eq. (17.28).

The cylindrical surface geometry appears particularly apt to describe sputtering in the electronic energy deposition regime, and for heavy projectiles, which fly on a straight line into the target. In fact, the quadratic dependence of Eq. (17.42) has been observed in several experiments, such as the sputtering of molecular solids under MeV light projectiles (Johnson, 1990; Johnson and Sundqvist, 1992; Johnson and Schou, 1993).

(ii) *Phase-explosion* or *gas flow* models: The idea that a high energy-density region may reach temperatures beyond the critical temperature T_c of the liquid-gas phase transition appears to have occurred first in describing the sputtering of condensed-gas targets by keV ions (Michl, 1983). The sputter yield can then be described by the competition of heat conduction, which freezes the volume of high energy density, and the thermal flow velocity which drives the high-pressure, high-temperature gas out of the high-energy-density zone into the vacuum and leads to sputtering (Kelly, 1990; Reimann, 1993; Miotello and Kelly, 1997). This idea has been used to quantitatively describe the sputtering of weakly bound systems in a variety of cases (Urbassek and Michl, 1987; Balaji et al., 1990, 1995).

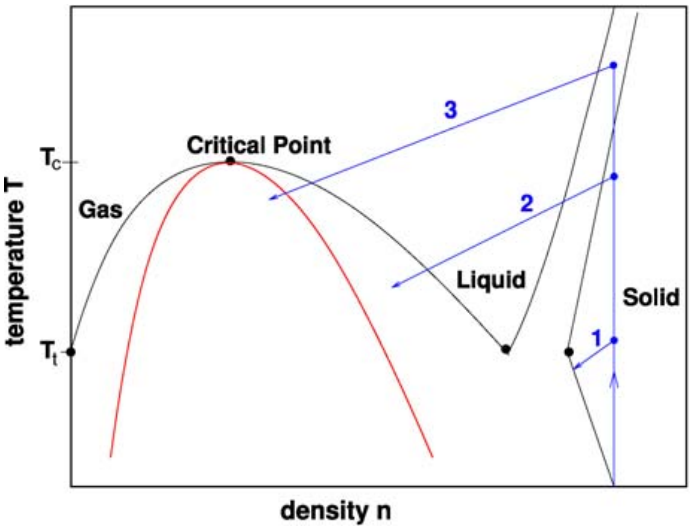

Fig. 17.10. Schematics of the phase-explosion model of spike sputtering. The temperature-density phase diagram of a model material is outlined. Triple-point temperature T_t and critical temperature T_c are indicated. The spinodal line, separating the metastable part of the liquid-gas coexistence region from the unstable part is indicated (color online: red). Schematic temperature-density trajectories of the energized spike volume are displayed (color online: blue). Trajectories 1–3 correspond to increased deposited energy densities. Trajectory 1 does not contribute to sputtering, while 2 enters the liquid-gas coexistence region and starts (non-equilibrium) surface evaporation. Trajectory 3 even passes the spinodal: The unstable material will spontaneously start boiling (*phase explosion*).

As Fig. 17.10 shows, the phase-space trajectory of a suddenly (isochorically) heated volume element may pass after (adiabatic) expansion deep into the liquid-gas coexistence region. If the spinodal line (defined such that the material inside the spinodal is unstable and immediately starts to undergo phase separation) is approached, the system will start bulk boiling; this process has been termed *phase explosion*. This model has also been invoked to explain the high abundance of large-mass clusters sputtered under spike conditions (Urbassek, 1988): If the trajectory passes close to the critical point, the material will decompose into a mixture of clusters of all sizes following a power law in cluster size n, Eq. (17.41), with δ given by a critical exponent, $\delta = 7/3$.

(iii) *Shock-wave* and *pressure-pulse* models: These models emphasize that the high energy density in the spike region leads not only to a high temperature, but also to a large pressure in this volume. The pressure gradient to the surrounding material, and in particular to the vacuum above the surface, will induce a pressure pulse or shock wave, which may lead to sputtering when it unloads at the surface. Depending on the details of the modelling, a dependence of the yield $Y \propto (\mathrm{d}E/\mathrm{d}x)^n$ with $n = \frac{3}{2}$ or 3 is obtained (Kitazoe et al., 1981; Bitensky and Parilis, 1987; Johnson et al., 1989; Reimann, 1995).

Energy distributions of sputtered particles typically exhibit a broad low-energy maximum at energies $E \ll U$, see Fig. 17.11. This maximum is attributed to thermal processes occurring at the spike temperature. Both surface-evaporation and phase-explosion models predict the maximum to be at energies in the range of $E = kT$, where T is a temperature between the boiling temperature T_b and the critical temperature T_c of the target, and

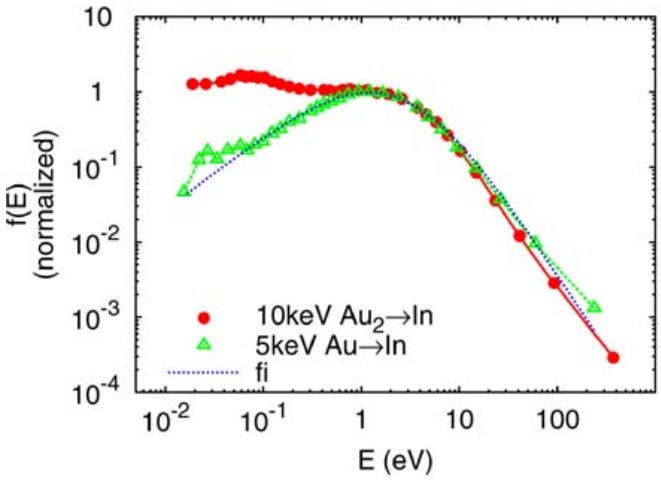

Fig. 17.11. Kinetic energy distributions of neutral In atoms sputtered from a polycrystalline In sample under impact of a Au atom (triangles) and a Au_2 dimer (circles). The impact energy is in both cases 5 keV/atom. The fit to a Thompson distribution of linear-cascade theory, Eq. (17.38), describes well the case of atom bombardment, but not the excess of low-energy atoms which are sputtered by dimer impact. Data taken from Samartsev et al. (2005).

k is Boltzmann's constant. Thus, an experimental energy spectrum like that of 10 keV Au_2 impact into In (Fig. 17.11) can be interpreted to be due to two different mechanisms: a linear-cascade contribution operative at energies $E > 1$ eV, which is well described by the Thompson distribution, Eq. (17.38), and an additional spike distribution, which is responsible for the excess of low-energy atoms ($E < 1$ eV).

17.3.2. Cluster impact

When a cluster impinges on a surface, it will break up into its constituent atoms; each of these will deliver its energy in the solid. At sufficiently small energies the total cluster energy will hence be delivered in a roughly hemispherical volume, and the deposited energy density can reach high values; this constitutes an ideal setting for spike sputtering. At higher bombarding energies, the stochastics of energy deposition and scattering may lead to an only incomplete overlap of the individual collision cascades. Bouneau et al. (2002) and Bouneau et al. (2002) illustrated the huge sputtering yields which may be achieved as a consequence of cluster impact in a series of beautiful experiments performed with Au_n clusters ($n = 1$–13) bombarding a Au target, see Fig. 17.13.

At smaller projectile energies, molecular-dynamics simulation is an adequate tool to analyze the effects of cluster impact (Colla et al., 2000). Figure 17.9 displays the results of a Au_8 impact on a Au surface at 16 keV/atom impact energy, i.e., around the lowest energies where experiments have been performed. The simulation results show that the sputtering process corresponds to a *phase explosion*, in which sputtering occurs by the gasification of the high-energy-density zone, as long as this is situated sufficiently close to the surface (cf. Section 17.3.1, item (ii)). In the bombardment of metallic targets under spike conditions, late ejection of large clusters (droplets, containing some 1000 atoms) is observed (Colla et al., 2000), cf. Fig. 17.9. These were emitted as compact 'fingers'

(Nordlund et al., 2003), which remained as protrusions left over the violent disruption of the surface; their fate is decided by the interplay of surface tension pulling the fingers back towards the surface and the drift velocity which the fingers obtained during the 'explosion' of the highly pressurized spike region.

17.3.3. Crater formation

The formation of a crater under heavy-ion or cluster impact has been observed repeatedly in computer simulation. For Cu cluster bombardment of a Cu surface, and analogously also for Au, with energies of the order of 10 keV per cluster, large craters were observed in molecular-dynamics simulations (Aderjan and Urbassek, 2000; Colla and Urbassek, 2000; Bringa et al., 2001). In these cases it was found that about half of the atoms that left the crater were sputtered; the other half was deposited on the surface in the form of a crater rim.

Nordlund et al. (2001) investigated the dependence of the size of ion-induced craters on the materials properties of the target. They could show that the crater size scales inversely proportional to the cohesive energy and to the melting temperature of the material. Nordlund et al. (2003) identified various macroscopic features connected to crater production by <100 keV atom and cluster impact on heavy metals (Ag and Au). Similarly as in experiment (Birtcher and Donnelly, 1996; Donnelly and Birtcher, 1997), they find the craters produced to be often of a highly asymmetric form, accompanied by adatom ridges extending far from the crater itself. These structures are due to the random arrangement of protuberances ('fingers') at the crater rim.

17.3.4. Linear vs nonlinear sputtering

The sputter yield formula (17.28) describes *linear* sputtering, in the sense that the sputter yield is proportional to the stopping power of the ion. For cluster impact, another concept of linear or *additive* sputtering is useful, which can be introduced by comparing the two following experiments:

(i) An n-atom cluster with total energy E impacts on the target and sputters Y_n atoms.
(ii) n single atoms of energy E/n bombard the surface completely independently, e.g., at widely different locations. Each atom has a sputter yield Y_1.

Then if

$$Y_n(E) = n \cdot Y_1(E/n), \tag{17.43}$$

the two experiments give identical results: Cluster impact has no 'synergistic' effect. Such a behavior has been called additive sputtering (Anders et al., 2004), since each atomic constituent of the cluster contributes equally and additively to the total sputter yield. Doubling the projectile size for the same velocity will hence double the sputter yield.

A closer analysis of this additive sputter law has been performed for the self-bombardment of a Lennard-Jones solid by clusters of size $n = 4$–10^4 (Anders et al., 2004). These simulations were performed at relatively small energies, such that the energy deposition occurs close to the target surface. The data shown in Fig. 17.12 align well on a single line given by Eq. (17.43) with

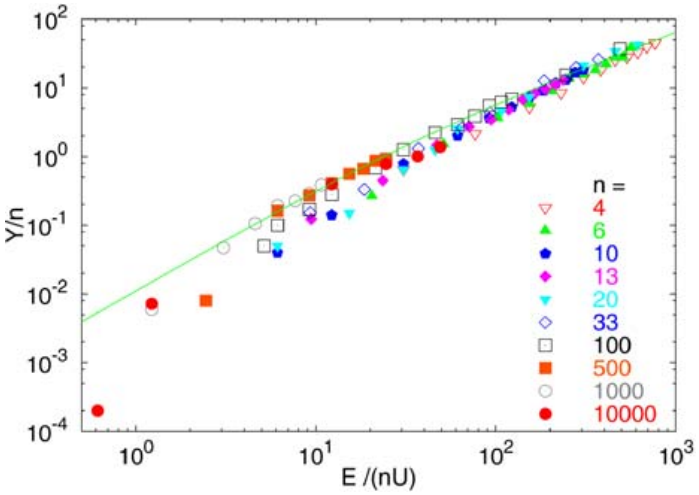

Fig. 17.12. Synoptical display of sputter yield Y vs scaled bombarding energy $\epsilon = E/U$ for projectile clusters of various size n, see legend. A fit function according to Eq. (17.44) with parameters $\alpha = 0.065$, $b = 0.5$ and $x_c = 33.6$ describes the data reasonably well, in particular for higher energies $E/nU \gtrsim 10$. Data taken from Anders et al. (2004).

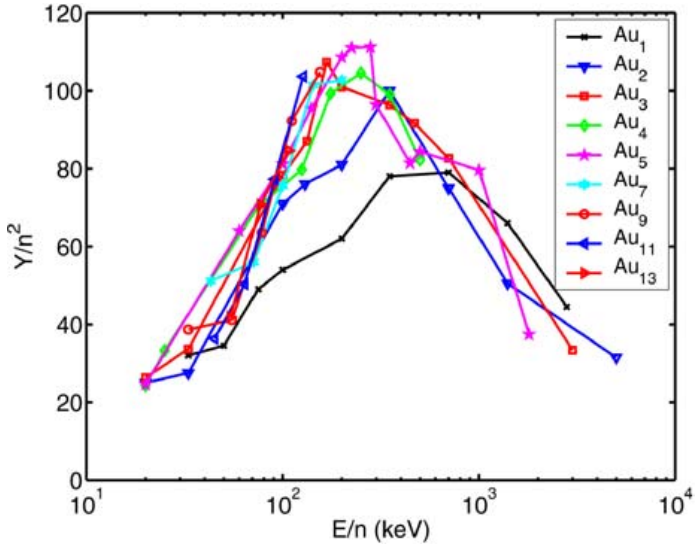

Fig. 17.13. Experimental sputter yields Y of Au sputtered by Au_n clusters of energy E. The data for $n > 2$ show a scaling like $Y = n^2 f(E/n)$, Eq. (17.45). Data taken from Bouneau et al. (2002).

$$f(x) = \alpha \frac{x^{1+b}}{(x_c + x)^b}. \tag{17.44}$$

Thus, sputtering has been found to become linear with projectile energy per atom in this system above a threshold, $E \gg x_c nU$.

Cluster-induced sputter yields Y of Au sputtered by Au_n clusters of energy E have been measured over a wide range of energies and cluster sizes by Bouneau et al. (2002), cf. Fig. 17.13. The data exhibit a scaling like

$$Y_n = n^2 f(E/n), \tag{17.45}$$

i.e., sputtering is not additive but pronouncedly nonlinear. Note that monomer and – to a lesser degree – dimer impact does not yet fulfill this scaling completely, which is however astonishingly well fulfilled for clusters with sizes $n = 3$–13. A convincing argument for Eq. (17.45) is still missing.

17.4. Ablation of metals by ultrafast laser pulses

The physical processes occurring in a material irradiated by an intense laser beam strongly depend on the type of material (insulator or metal), the laser frequency and intensity, and the laser pulse duration. In this paper, I shall focus on ultrashort laser pulses in the picosecond or femtosecond regime since here the analogy to ion-beam sputtering is most evident. Several of the processes complicating the physics of nanosecond laser pulse ablation – plasma formation, laser interaction with the ablation cloud, expansion physics of the ablation cloud, cluster aggregation and fragmentation in the cloud – will be sketched in Section 17.4.3. We shall focus on metallic targets irradiated by visible or UV lasers where the laser energy is absorbed in the electronic system and then transferred to the atomic system.

In the case of insulators, where the band gap is wider than the photon energy, the material is transparent to the radiation. The light is hence only absorbed within the volume of the material, and ablation starts only after a first few incubation pulses which induce defect formation and the ensuing decomposition of the material (Bäuerle, 2000).

Ultrafast laser ablation shows advantages in applications over ns-pulse ablation, since the "heat affected zone" which shows signs of damage due to melting is reduced or avoided, and wide-band-gap materials can be processed due to multi-photon processes.

17.4.1. From energy absorption to the two-temperature model

17.4.1.1. Light absorption

The typical setup considered in this section is the excitation of a metal by a femtosecond or picosecond laser pulse in the visible or UV regime. When laser light with intensity I_0 shines on a metal surface, a fraction R is reflected, while the remainder is absorbed inside the material. The absorbed intensity I follows an exponential attenuation law

$$I(z,t) = (1-R) I_0(t) e^{-z/\ell} \tag{17.46}$$

with the attenuation length ℓ. Here z measures the depth into the solid. Both the reflection coefficient R and the absorption length ℓ are a function of the laser frequency ω. In particular, for frequencies above the plasma frequency, $\omega > \omega_p$, the metal becomes transparent, $R \to 0$ and $\ell \to \infty$. For metals, the plasma frequency is in the UV; in this contribution we shall only consider the case $\omega < \omega_p$. The attenuation length is given by the skin depth

$$\delta = \sqrt{\frac{2}{\mu\sigma\omega}} \tag{17.47}$$

where $\sigma = \sigma(\omega)$ is the AC conductivity of the metal, and μ its permeability. For example, Au has $R = 0.47$ and $\ell = 22$ nm for 500 nm incident light (Bäuerle, 2000).

This energy deposited in the conduction electron system will thermalize internally on a time scale of a few femtoseconds; the details of this process have been analyzed by Rethfeld et al. (1999, 2002a).

Electrons may be excited in the conduction band up to energies $\hbar\omega$ above the Fermi energy. From Fermi liquid theory (Pines and Nozières, 1966) and two-photon photoemission experiments (Aeschlimann et al., 1996) it is known that the lifetime of an excited electron is limited by electron–electron collisions and decays like $1/(\Delta E)^2$ with the height of the electron energy $\Delta E = \hbar\omega$ above the Fermi level. Thus, high-energy non-thermalized electrons can penetrate far into the solid from the laser absorption regime; since these electrons run on straight trajectories, unlike diffusion, they are termed *ballistic* electrons.

17.4.1.2. Two-temperature model

After thermalization, the electron energy is dissipated by diffusion deeper into the metal, and by electron–atom collisions to the atomic system of the metal. These processes are conveniently summarized in the so-called two-temperature model, which assumes that the electronic system and the atomic system have two separate temperatures T_e and T_a, respectively, which equilibrate in the course of time. This model has originally been developed by Anisimov et al. (1974) to describe the processes occurring in a metal after swift-ion impact in the electronic-stopping regime, cf. Section 17.2.1.4 above. However, it has now been applied with great success to describe the ultra-short laser irradiation of metals. The model is described by the following equations:

$$C_e \frac{\partial T_e}{\partial t} = \frac{\partial}{\partial z} \Lambda_e \frac{\partial T_e}{\partial z} - g(T_e - T_a) + Q(z,t), \tag{17.48}$$

$$C_a \frac{\partial T_a}{\partial t} = g(T_e - T_a). \tag{17.49}$$

Here, the source term

$$Q(z,t) = \frac{1}{\ell} I(z,t) \tag{17.50}$$

has been used. The various terms and coefficients appearing in Eqs. (17.48) and (17.49) will now be discussed.

The atomic (volumetric) specific heat C_a is taken as $3kn$ according to the Dulong–Petit law, where n is the atomic number density and k is Boltzmann's constant; in numerical treatments, such as the molecular-dynamics study of Ivanov and Zhigilei (2003), better estimates are available.

The electronic specific heat is proportional to T_e as

$$C_e(T_e) = \gamma T_e. \tag{17.51}$$

The constant γ is in many cases well described by Sommerfeld's result $\pi^2 n_e k/(2T_F)$, where n_e is the electron density and T_F is the Fermi temperature. For Au, it is $\gamma = 67.6\ \mathrm{J/m^3\,K^2}$ and $T_F = 6.4 \times 10^4$ K. We note that Eq. (17.51) holds true for temperatures $T_e \ll T_F$ only.

The coefficient g has been termed the *electron–phonon coupling* coefficient, even though it is applied also in cases where the atomic system has already molten. Typical values range from 21–360 $\mathrm{GW/K\,cm^3}$; these values represent Au and Ni, respectively, as examples of a weakly and a strongly coupled metal. The dependence of g on T_e and T_a is not known, and even its value at room temperature is not well measured. For Cu, for example, a recent compilation (Bonn et al., 2000) quotes literature values between 10 and 200 $\mathrm{W/K\,cm^3}$.

17.4.1.3. Electronic heat conduction

The *lattice* heat conduction can be ignored in good approximation, as it is small compared to the electronic heat conduction. The *electronic* heat conduction, however, is important. It has been discussed intensely by Anisimov and Rethfeld (1997). They propose a functional dependence

$$\Lambda_e = \alpha \frac{({\theta_e}^2 + 0.16)^{5/4}({\theta_e}^2 + 0.44)\theta_e}{({\theta_e}^2 + 0.092)^{1/2}({\theta_e}^2 + \beta\theta_a)}, \tag{17.52}$$

where $\theta_a = T_a/T_F$ and $\theta_e = T_e/T_F$. For Au, the parameters in Eq. (17.52) assume values $\alpha = 353\ \mathrm{W/K\,m}$ and $\beta = 0.16$.

Expression (17.52) is valid over a wide range of temperatures, in particular also when T_e approaches (or exceeds) the Fermi temperature (Anisimov and Rethfeld, 1997). For smaller T_e, Eq. (17.52) can be simplified to (Wang et al., 1994)

$$\Lambda_e = \frac{AT_e}{a{T_e}^2 + bT_a}. \tag{17.53}$$

This expression models the gas-kinetic heat conduction, which is proportional to $C_e(T_e)/\nu$. The collision frequency ν has contributions from electron–electron and electron–atom scattering, which are described by the terms aT_e^2 and bT_a, resp. For Au, it is $A = 4.35 \times 10^{13}\ \mathrm{W/K\,s\,m}$, $a = 1.2 \times 10^7/\mathrm{s\,K^2}$, and $b = 1.23 \times 10^{11}/\mathrm{s\,K}$.

Figure 17.14 illustrates this dependence. Above the Fermi temperature of Au, Λ_e strongly increases, since Coulomb collisions become inefficient in a high-temperature plasma. The maximum observed in Fig. 17.14 reflects the competition of the increase of specific heat with temperature and the hindrance of transport by electron–electron collisions.

Note that the high electronic heat conductivity smears the laser attenuation profile Eq. (17.46) to considerable higher depths and acts as a heat source for atoms. Since electronic heat conduction is quick, and electron–phonon coupling is slow, the processes of electronic energy dissipation and heat transfer to the atoms may be considered decoupled to a good approximation.

17.4.1.4. Example: Instantaneous homogeneous excitation

We will illustrate the characteristic features of the two-temperature model with the help of a simple example. Consider a free-standing thin film; when its electronic system is instantaneously energized by a femtosecond laser pulse, ballistic electrons will homogenize the electron energy quickly throughout the film. Thus assume that at time $t = 0$ an energy E_0 has been given to the electrons such that they acquire a temperature T_0, which is large

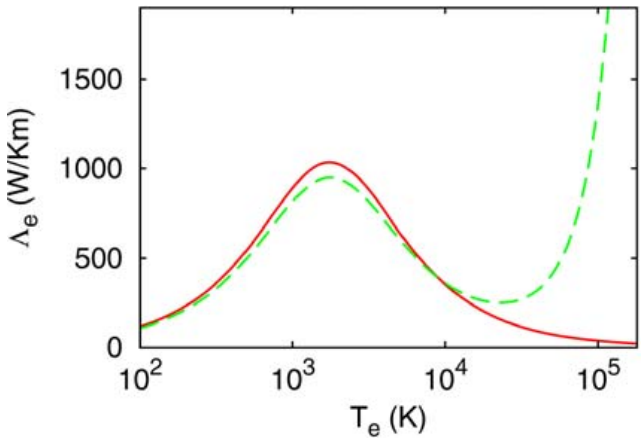

Fig. 17.14. Electronic heat conductivity Λ_e in Au as a function of the electron temperature T_e for fixed atom temperature $T_a = 300$ K. The complete expression (17.52) (full line) is compared to the approximation (17.53) (dashed) valid below the Fermi temperature $T_F = 6.4 \times 10^4$ K.

compared to the lattice temperature. Then, as long as $T_e \gg T_a$, the solution of Eqs. (17.48) and (17.49) reads

$$T_e = T_0\left(1 - \frac{t}{\tau}\right), \qquad T_a = T_\infty\left[2\frac{t}{\tau} - \left(\frac{t}{\tau}\right)^2\right], \tag{17.54}$$

and hence

$$E_e = E_0\left(1 - \frac{t}{\tau}\right)^2, \qquad E_a = E_0 - E_e, \tag{17.55}$$

where the relaxation time

$$\tau = \frac{\gamma}{g}T_0 = \sqrt{\frac{2\gamma}{g}E_0} \tag{17.56}$$

and the final atom temperature

$$T_\infty = \frac{E_0}{C_a} \tag{17.57}$$

have been introduced. The results hold for $t \ll \tau$.

The temperature evolution and the resulting energy evolution in the electronic and atomic system are displayed in Fig. 17.15. It is seen that the electron temperature initially reaches very high values due to the small electronic heat capacity. After thermalization, however, for the same reason, almost all the energy has been transferred to the atomic system.

17.4.2. Materials effects

17.4.2.1. Overview

Figure 17.16 illustrates the materials effects to be expected in a metallic target irradiated with increasing laser fluence. These results from a molecular dynamics simulation

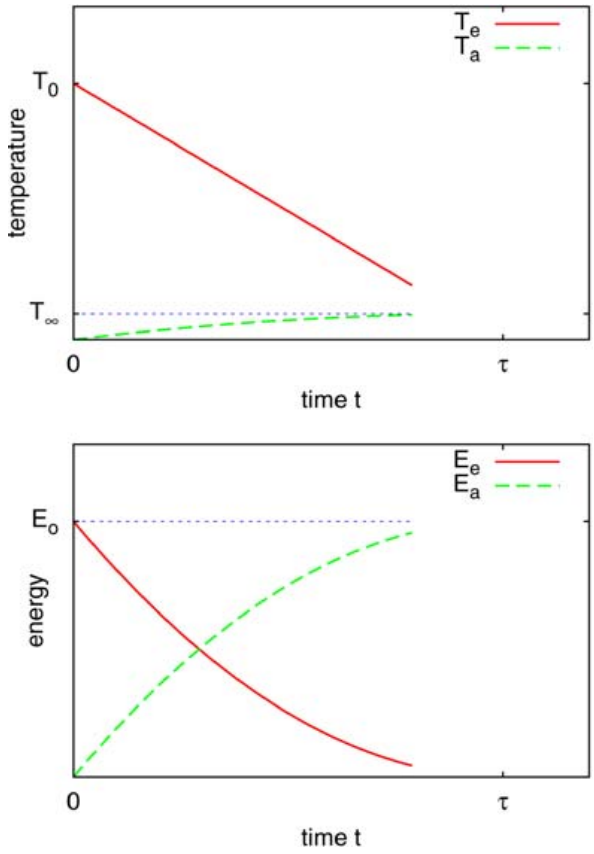

Fig. 17.15. Temporal evolution of temperatures (top) and energies (bottom) in the atomic and electronic subsystem of an ultrafast laser-excited metal. The simplified analysis, Eqs. (17.54) and (17.55), holds as long as $T_e \gg T_a$, and hence for times $t \ll \tau$. Here τ is the relaxation time of the system, Eq. (17.56), determined by the materials parameters and the initial energy input E_0. This figure demonstrates that in spite of the extremely high electronic temperatures reached, the laser energy efficiently dissipates into the atomic system.

have been calculated for computational convenience for a thin-slab geometry, in which the atoms can be assumed to be instantaneously and homogeneously energized. The energy, which each atom receives from the laser, is denoted the so-called 'energization' E_0. We see that with increasing E_0 the material starts melting, then voids nucleate, which finally lead to the thermomechanical spallation of the metal; at the highest energies shown the material gasifies into a vapor cloud, containing monomers and clusters of various sizes. Note that with increasing laser fluence the probability of electron emission from the metal and ionization of emitted atoms and clusters will increase, and hence actually a plasma may form; this process had not been included in the simulation underlying Fig. 17.16.

The phenomenon of *non-thermal* or *cold* melting has been discussed for insulating and semi-conducting systems for a while (Stampfli and Bennemann, 1990; Graves and Allen, 1998; Jeschke et al., 2001). In these systems, for sufficiently high electronic excitation density, electrons are excited out of their covalent bonding states to non-bonding or antibonding orbitals. This change in the potential energy of the solid induces forces on the atoms, and hence disordering of the lattice, before the electron–phonon coupling mechanism of the two-temperature model energizes the atoms. However, thermal melting can

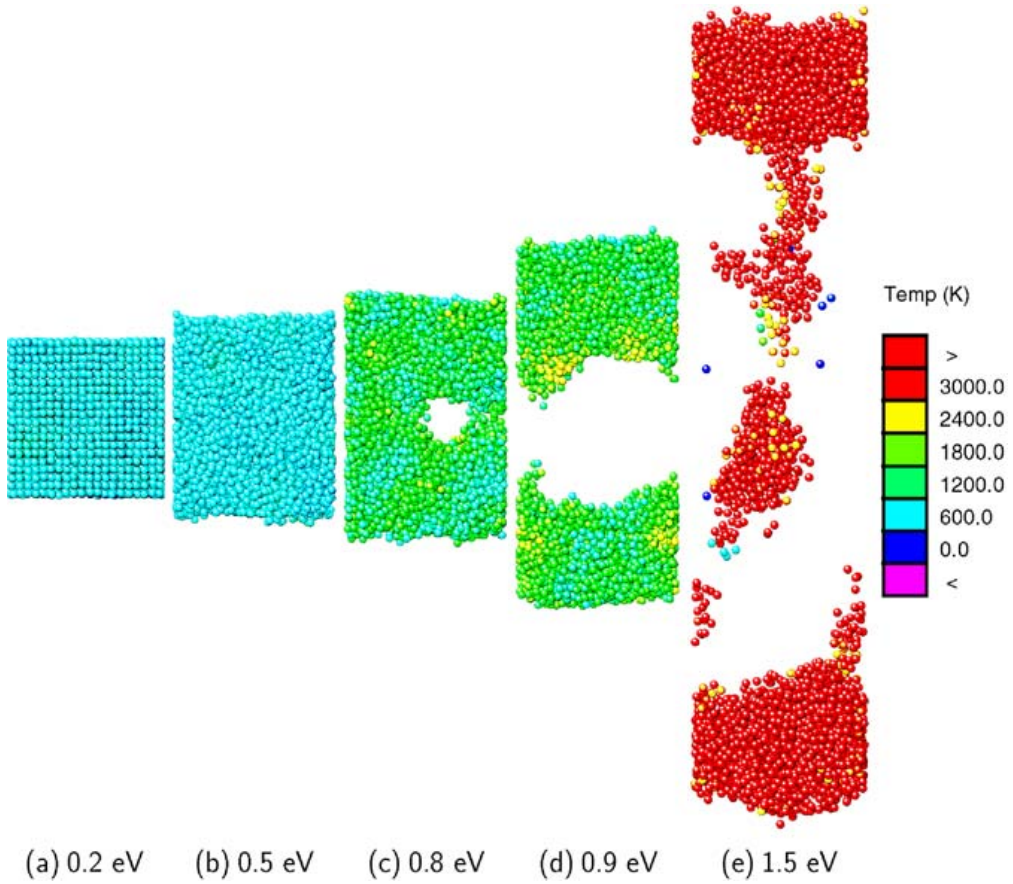

Fig. 17.16. Series of snap shots of a short-pulse laser-irradiated Al film featuring various materials processes. All figures taken at 5 ps after irradiation. The energy E_0 which each atom receives from the laser is denoted at the bottom. The expansion of the system due to the increased energy input is clearly observable. Gray-scale (color online) denotes the local temperature. (a) Material is heated, but remains crystalline. (b) Material melts. (c) A void forms temporarily. (d) The film breaks (thermomechanical spallation). (e) Cluster formation.

also occur ultrafast, i.e., within a few ps, if a sufficiently large superheating (of the order of $T \cong 1.5T_m$ is achieved (Rethfeld et al., 2002b).

The laser ablation of molecular substrates with increasing energization occurs in close analogy to the processes in metals mentioned above. Zhigilei et al. (2003) enumerate the following ablation mechanisms, which they analyzed in detail from the molecular-dynamics simulation of the laser ablation of molecular substrates: surface desorption, overheating and phase explosion, photomechanical spallation, photochemical ablation.

Figure 17.17 shows the materials processes occurring after laser irradiation in a temperature-density phase diagram. In analogy to previous simulational work by Zhakhovskii et al. (2000), Perez and Lewis (2002, 2003) and others, this presentation allows to obtain an overview of how increasing laser fluences lead to different materials effects, in analogy to the real-space atomistic snap shots shown for Al in Fig. 17.16. The following sequence of processes is visible:

(i) heating in the crystalline state,
(ii) melting,

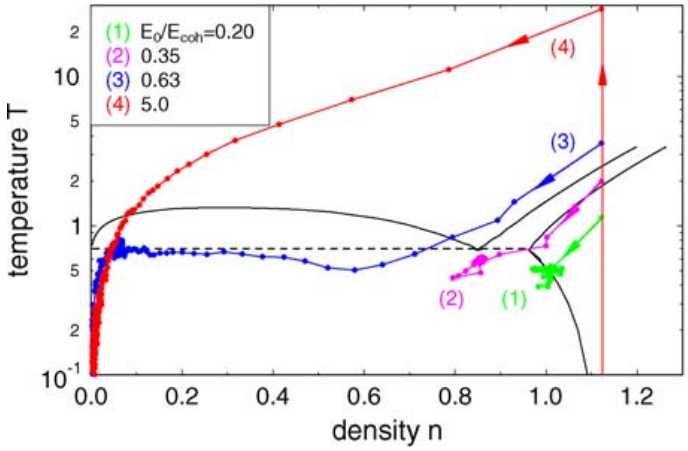

Fig. 17.17. Laser-irradiation-induced processes in a van-der-Waals solid. The phase diagram of a Lennard-Jones material is outlined. Trajectories 1–4: Temperature-density trajectories of a Lennard-Jones solid, suddenly excited to an energy/atom of E_0, measured relative to the cohesive energy E_{coh}. The trajectories are calculated by a molecular-dynamics simulation for a slab of 30 monolayers thickness and present averages over the central third part of the system. The sudden excitation leads to a rapid isochoric temperature increase, followed by a rapid expansion and cooling. At small energies this process ends with target melting, at higher energies the solid- (or liquid-) vapor coexistence region is entered and the material fails by spallation or complete vaporization. The analogous processes for a laser-irradiated *metal* are visualized atomistically in Fig. 17.16.

(iii) void formation and collapse,
(iv) complete target disintegration and cluster formation.

We note that for larger simulation crystallites, the process of target melting does not occur (Anisimov et al., 2003; Inogamov, 2006); this is a consequence of the small liquid regime in van-der-Waals solids. Note the analogy of the processes occurring under laser ablation to those of sputtering in a spike scenario, cf. Fig. 17.10.

17.4.2.2. Thermomechanical spallation

The thermoelastic pressure induced by the deposited energy density leads to thermomechanical effects in the sample. Paltauf and Dyer (2003) These result in particular from the tensile pressure which originates due to the interaction of the initially compressive pressure with the free sample surface. The process occurring at the ablation threshold has been termed *thermomechanical spallation*. Spallation may be defined as the rupture of a sample due to a strong tensile pressure, such as it occurs due to pressure and shock waves induced by projectile impacts, explosions, or laser pulses (Vidal et al., 2004). Alternatively, the process of vapor-bubble formation in liquids is termed *cavitation*, or the generic term *fragmentation* may be employed (Vogel and Venugopalan, 2003).

The spallation mechanism can be illustrated by a molecular-dynamics simulation, Fig. 17.18. This simulation was performed close to the ablation threshold in Cu, at a laser fluence of 170 mJ/cm^2 and a laser pulse width of 0.5 ps. Simultaneously with the atomic motion simulated by molecular dynamics, the electron heat transport and energy transfer between the electronic the and atomic system was taken into account by a finite-difference solution of the electron temperature equation, Eq. (17.48). Figure 17.18 shows that at the time of spallation a strongly negative tensile pressure has developed with peak values of

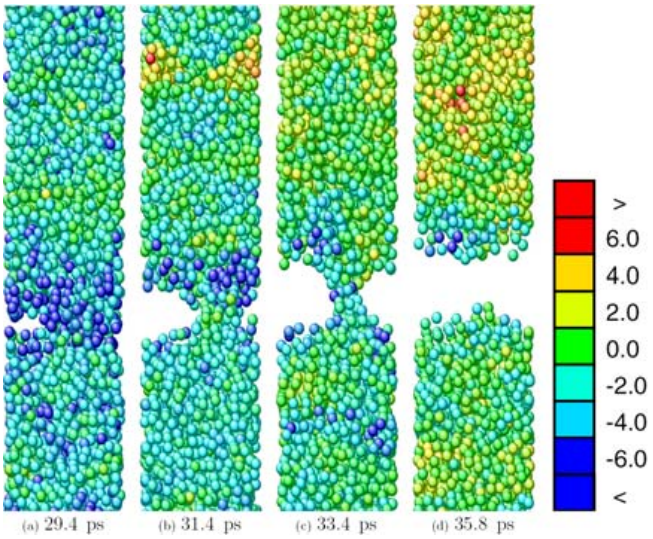

Fig. 17.18. Atomistic view of the spallation process in a Cu crystal irradiated at time $t = 0$ by a 0.5 ps laser pulse of a fluence of 170 mJ/cm^2. Results of a molecular-dynamics simulation (Schäfer, 2001; Schäfer et al., 2002). The series of snapshots shows only the relevant part of the crystallite, where fracture occurs at times around 32 ps after the irradiation. The target surface is not visible. The cross sections shown have a height of 60 Å and a width of 21 Å; they are 10 Å thick. Atoms are gray-shaded (color online) according to their local pressures in GPa. Fracture occurs at a depth of 20 nm, which is beyond the laser attenuation length of 14 nm.

the order of -6 GPa. Since the system has already molten by this time, the liquid cannot sustain the large tensile pressure peak and tears.

Thus the main result of this and similar simulations (Leveugle et al., 2004; Vidal et al., 2004) has been to show that it is not only the absorbed energy density which defines the ablation threshold; also pressure is an important variable, and it is in particular the tensile pressure which develops in the molten target, which leads to thermomechanical spallation, and hence ablation.

17.4.2.3. Pressure wave

The origin of the tensile pressures developing in the solid can be clarified using the analysis of Bushnell and McCloskey (1968) and Dingus and Scammon (1991). An exponential energy deposition profile, analogous to Eq. (17.46), will establish a similar compressive pressure profile

$$p(z) = \Gamma \frac{\Phi_0}{\ell} e^{-z/\ell}, \tag{17.58}$$

where Φ_0 is the surface value of the absorbed fluence and Γ is the Grüneisen coefficient. The latter is a materials constant which relates the induced thermoelastic pressure to the absorbed energy density; its value is around 2, but shows a slight temperature dependence (Slater, 1940; Zel'dovich and Raizer, 1966). The inhomogeneous pressure distribution will send a compressive wave into the target inner. Note, however, that the initial thermoelastic pressure is highest at the surface: this is an unstable situation, since mechanical equilibrium requires $p = 0$ at the surface. The material responds by *unloading* at the surface; this means that the surface expands into vacuum and a second, so-called *rarefaction wave* is

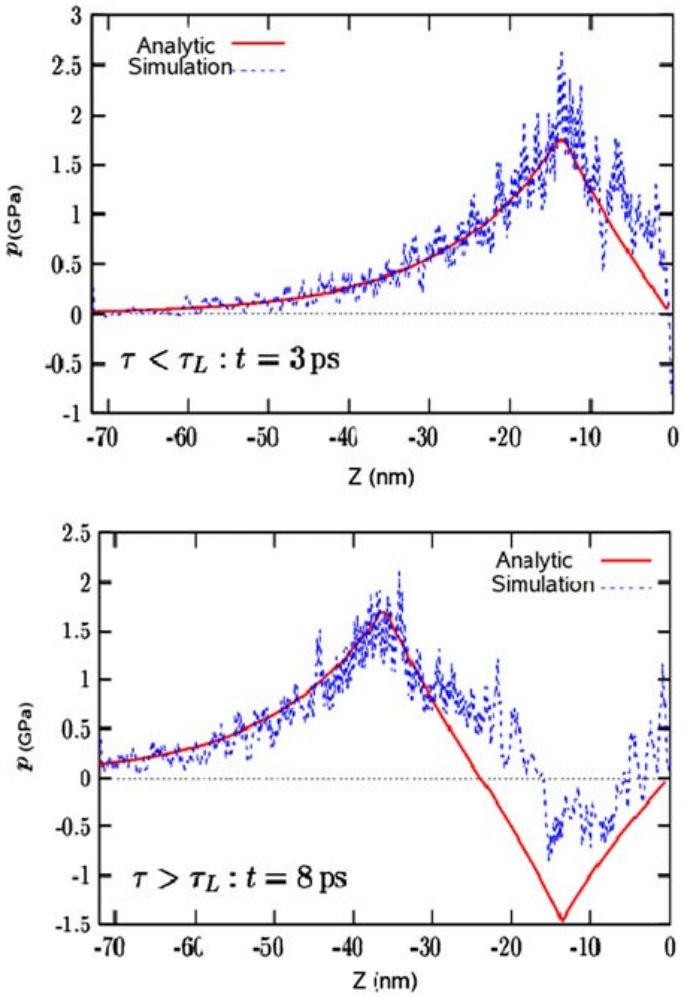

Fig. 17.19. Laser-irradiation-induced pressure wave in a Cu crystallite: Results of a molecular-dynamics simulation (Schäfer, 2001). The crystallite has been irradiated with a laser pulse of duration $\tau_L = 5$ ps with a fluence of 20 mJ/cm^2, and an exponential absorption profile, Eq. (17.46), with absorption length $\ell = 14$ nm. The figure shows the resulting pressure profile during (top) and after (bottom) the pulse. The data are compared to an analytical expression of the pressure profile given by Bushnell and McCloskey (1968) and Dingus and Scammon (1991), where the sound velocity has been assumed to $c = 45$ Å/ps and the Grüneisen constant to $\Gamma = 1.2$.

sent into the target inner. The resulting wave thus has a bipolar struction, where the first compressive peak is followed by a tensile pressure peak, cf. Fig. 17.19. It is the second tensile peak which has catastrophic materials consequences, in particular when the target is molten and thus has a small yield strength.

17.4.2.4. Ablation yield and threshold

Figure 17.20 shows the ablation rate measured under short-pulse laser irradiation of Cu (Preuss et al., 1995; Nolte et al., 1997). An ablation threshold at a fluence of $\Phi_{\rm th} =$ 140–170 mJ/cm^2 is observed. This figure also compares to molecular-dynamics computer simulation results, which observe the threshold at a similar value, $\Phi_{\rm th} = 170$ mJ/cm^2. The threshold in the simulation is sharp; above $\Phi_{\rm th}$, a sizeable amount of material, between

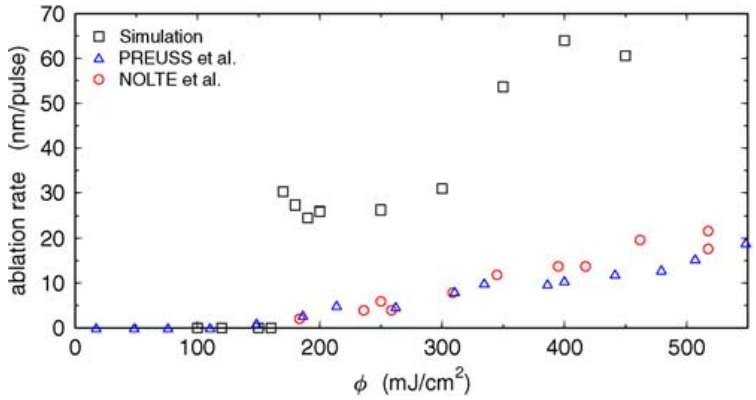

Fig. 17.20. Ablation rate versus fluence for short-pulse laser irradiation of Cu. ◯: Experiment by Nolte et al. (1997), at a wavelength of 780 nm and a pulse duration $\tau_L = 0.15$ ps. △: Experiment by Preuss et al. (1995) at a wavelength of 248 nm and $\tau_L = 0.5$ ps. □: Simulation results for $\tau_L = 0.5$ ps by Schäfer et al. (2002).

20 and 30 nm, is ablated. This is due to the spallation mechanism described above, Section 17.4.2.2. Experiment, however, shows only small ablation rates above the threshold, of the order of a few nm/pulse. It is believed that this is due to the measurement technique, which involves of the order of 1000 shots to measure the ablation rate; hence, irradiation-induced surface modification may influence the results (Schäfer et al., 2002).

The existence and size of an ablation threshold Φ_{th} as well as the fluence dependence of the yield above the threshold can be derived using the following argument, which will be presented in its simplest form valid for insulators (Brannon et al., 1985; Johnson, 1994). Here it is assumed that the *energy* density deposited by the laser

$$\Phi(z) = \Phi_0 e^{-z/\ell} \tag{17.59}$$

determines the ablation process. Φ_0 is the absorbed fluence at the surface. Assuming that ablation occurs if the local energy density, $\epsilon(z) = \Phi(z)/\ell$, increases above a critical value, ϵ_c, Eq. (17.59) leads to an ablated depth of

$$z_{\text{abl}} = \ell \cdot \ln \frac{\Phi}{\Phi_{\text{th}}}, \tag{17.60}$$

where the ablation threshold is given by

$$\Phi_{\text{th}} = E_c \ell. \tag{17.61}$$

Note that in metals the electronic heat conduction will spread the profile, hence effectively increasing ℓ. Furthermore, the two-temperature equations (17.48) and (17.49) have to be taken into account, cf. Bäuerle (2000), p. 271f; these consideration do not seriously change the result (17.61).

17.4.3. Further effects: Longer laser pulses and post-emission effects

In this contribution I concentrated on those aspects of laser ablation which show the most similarities to ion sputtering in the spike regime. However, due to the wide variability of

laser frequencies, pulse length, and the materials involved, fascinating physical processes are involved, which I briefly mention below. For a fuller coverage of this subject the reader should consult reviews like Phipps and Dreyfus (1993), Bäuerle (2000), Anisimov and Luk'yanchuk (2002), Georgiou and Hillenkamp (2003), Schou (2006).

(i) *Ablation mechanisms*: Beyond the essentially thermal ablation mechanism discussed in detail above, photons may directly break bonds in the target and thus induce *photochemical* ablation. Also, defects induced by the irradiation may lead to stresses or even to electrical fields inside the sample and thus induce material failure, i.e., ablation.

(ii) *Post-emission processes in the ablation cloud*: Immediately after ablation, the ablated material may still possess a rather high density, in particular for short-pulse ablation. Then, collisions in the gas cloud will be frequent. The consequences of these collisions are manifold: In the course of the adiabatic expansion process, internal energy will be converted into translational center-of-mass energy of the cloud. In other words, the cloud will internally cool, while its drift velocity off the surface increases. As a consequence, the energy distribution of ablated particles will change. This is of major importance for pulsed-laser deposition applications, since the properties of thin films formed from these particles may depend crucially on the particle energies involved (Chrisey and Hubler, 1994). Also the angular distribution will become more focussed, in the direction towards the target surface normal. Of course, these collision processes will be strongly changed, if the expansion is not into a vacuum, but into a background gas. Detailed hydrodynamic and also kinetic expansion models are available, which capture this physics quantitatively (Sibold and Urbassek, 1993; Anisimov et al., 1996; Anisimov and Luk'yanchuk, 2002).

(iii) *Clusters*: The flux of ablated particles consists not only of monomers, but also of clusters. Often, also droplets, i.e., large liquid clusters, are ablated. This cluster distribution will change due to the collision processes mentioned above, which induce both cluster agglomeration and fragmentation processes, and also due to cluster evaporation, which cools the clusters internally until a metastable equilibrium has been reached.

(iv) *A plasma may form*: Due to the interaction of the intense laser beam with the target, which may lead to the emission of both electrons and ions from the target, also the interaction of the laser beam with the ablation cloud will ionize it. Once a plasma has formed above the target, two main consequences arise: (i) The plasma may shield the target from the laser and thus reduce ablation. (ii) Due to internal electrical fields which are set up in particular at the plasma front, electrons and ions are strongly accelerated. While the plasma cloud in total is quasineutral, it obtains a pronounced internal structure, in which leading highly-charged ions are followed by singly-charged ions. Three-body recombination collisions may partly neutralize the plasma and thereby deliver potential energy to heat up and accelerate the plasma even more. As a consequence, the ions – and also the (re-neutralized) atoms – may reach kinetic energies, which are far above the thermal energies available from thermal processes. Thus, kinetic energies of above 1 keV have been measured for, e.g., the ablation of Ti by 80-fs pulses (Ye and Grigoropoulos, 2001).

17.5. Outlook

Research in the areas of solid erosion by ion or laser irradiation is an active field which is driven both by the development of new applications and by the analysis of fundamental aspects of the underlying mechanisms. In the following, I highlight some of the issues around which current research concentrates.

(i) While the phenomena of linear sputtering have been clarified, many aspects of nonlinear sputtering have still not been settled. What is the explanation of the surprisingly simple scaling in the measured data of nonlinear sputtering by cluster impact, Eq. (17.45)? Under which conditions is sputtering additive, i.e., is the sputter yield under molecule or ion impact equal to the sum of the sputter yields of the atomic constituents of the projectile?

(ii) What is the role of energy loss to the electronic system, both during the cascade, and in the thermal spike developing later? In a metal, electrons can quench the cascade quite rapidly, and hence freeze mixing processes in a compound and sputtering processes occurring from spikes. However, it is not clear how large the electron mean free path – and hence the heat conductivity – is in the strongly distorted underdense liquid spike region. This question has also immediate consequences for the yield of electronically excited and ionized sputtered particles.

(iii) A basic question of interest both in ion bombardment and laser irradiation is the validity of the interatomic empirical potentials used in the regime of high energy densities. While two-body potentials have been measured over the years with a high accuracy by spectroscopic and gas-phase-collision methods, the validity of many-body interaction potentials at high densities and temperatures is still yet poorly known. This applies even more, when simultaneously the electronic system has been highly excited.

(iv) Both in ion bombarded and laser irradiation, clusters are formed and even large chunks of matter (droplets) may be emitted from the target. Often, the abundance distribution of emitted clusters can be characterized by a power-law decay, Eq. (17.41). A quantitative understanding is still lacking.

(v) In the case of cluster impact into solids, the collision-cascade contribution to the sputter yield may be negligible compared to the contribution of the thermal spike involved. Here the analogy to the case of ultrashort laser irradiation appears to be most pronounced. Besides the different involvement of the electronic system, the lateral width of the energized zone, which is considerably larger for laser irradiation, forms the strongest difference.

(vi) For laser irradiation, the two-temperature model presents a sound basis to understand many aspects of ablation. Here the question of what happens before an electronic and an atomic temperature can be defined – i.e., before the corresponding subsystems have internally thermalized – is still open. Also, the processes occurring while the two subsystems are still in strong mutual non-equilibrium ($T_e \ll T_a$) strongly depends on the materials parameters adopted; their justification still awaits assessment.

(vii) The role of ballistic electrons transporting energy away from the irradiation zone needs to be implemented into a consistent picture of energy dissipation and ablation.

(viii) The thermodynamics and kinetics of the (non-equilibrium) phase transitions occurring under intense laser irradiation are fascinating. This applies in particular to the processes occurring around the ablation threshold (thermomechanical spallation in the liquid phase), but also to the regimes of phase explosion and plasma formation.

Acknowledgements

Thanks are due to Christian Anders, Cemal Engin, Yudi Rosandi, Christian Schäfer, Arun Upadhyay, and Steffen Zimmermann for preparing calculations and figures for this review, and to Michael Wahl, Klaus Wittmaack, and Andreas Wucher for providing original data. Discussions with Bärbel Rethfeld and Nail Inogamov on various issues connected to Section 17.4 are gratefully acknowledged.

References

Aderjan, R., Urbassek, H.M., 2000. Nucl. Instrum. Meth. B 164–165, 697.
Aeschlimann, M., Bauer, M., Pawlik, S., 1996. Chem. Phys. 205, 127.
Anders, C., Urbassek, H.M., Johnson, R.E., 2004. Phys. Rev. B 70, 155404.
Andersen, H.H., 1993. Mat. Fys. Medd. K. Dan. Vidensk. Selsk. 43, 127.
Andersen, H.H., Stenum, B., Sørensen, T., Whitlow, H.J., 1985. Nucl. Instrum. Meth. B 6, 459.
Anisimov, S.I., Kapeliovich, B.L., Perel'man, T.L., 1974. Sov. Phys. JETP 39, 375.
Anisimov, S.I., Luk'yanchuk, B.S., 2002. Phys. Usp. 45, 293.
Anisimov, S.I., Luk'yanchuk, B.S., Luches, A., 1996. Appl. Surf. Sci. 96–98, 24.
Anisimov, S.I., Rethfeld, B., 1997. Izvestia Akad. Nauk (Fiz.) 61, 1642.
Anisimov, S.I., Zhakhovski, V.V., Inogamov, N.A., Nishihara, K., Oparin, A.M., Petrov, Y.V., 2003. JETP Lett. 77, 606.
Averback, R.S., Diaz de la Rubia, T., 1998. In: Ehrenreich, H., Spaepen, F. (Eds.), Solid State Physics, vol. 51. Academic Press, Boston, p. 281.
Balaji, V., David, D.E., Magnera, T.F., Michl, J., Urbassek, H.M., 1990. Nucl. Instrum. Meth. B 46, 435.
Balaji, V., David, D.E., Tian, R., Michl, J., Urbassek, H.M., 1995. J. Phys. Chem. 99, 15565.
Bäuerle, D., 2000. Laser Processing and Chemistry, third ed. Springer, Berlin.
Betz, G., Husinsky, W., 1995. Nucl. Instrum. Meth. B 102, 281.
Betz, G., Kirchner, R., Husinsky, W., Rüdenauer, F., Urbassek, H.M., 1994. Radiat. Eff. Defects Solids 130–131, 251.
Biersack, J.P., Eckstein, W., 1984. Appl. Phys. A 34, 73.
Birtcher, R.C., Donnelly, S.E., 1996. Phys. Rev. Lett. 77, 4374.
Bitensky, I.S., Parilis, E.S., 1987. Nucl. Instrum. Meth. B 21, 26.
Bohdansky, J., 1984. Nucl. Instrum. Meth. B 2, 587.
Bonn, M., Denzler, D.N., Funk, S., Wolf, M., Wellershoff, S.-S., Hohlfeld, J., 2000. Phys. Rev. B 61, 1101.
Bouneau, S., Brunelle, A., Della-Negra, S., Depauw, J., Jacquet, D., LeBeyec, Y., Pautrat, M., Fallavier, M., Poizat, J.C., Andersen, H.H., 2002. Phys. Rev. B 65, 144106.
Brannon, J.H., Lankard, J.R., Baise, A.I., Burns, F., Kaufman, J., 1985. J. Appl. Phys. 58, 2036.
Bringa, E.M., Nordlund, K., Keinonen, J., 2001. Phys. Rev. B 64, 235426.
Brinkman, J.A., 1954. J. Appl. Phys. 25, 961.

Bushnell, J.C., McCloskey, D.J., 1968. J. Appl. Phys. 39, 5541.
Cheng, Y.-T., 1990. Mat. Sci. Rep. 5, 45.
Chrisey, D.B., Hubler, G.K. (Eds.), 1994. Pulsed Laser Deposition of Thin Films. Wiley, New York.
Colla, T.J., Aderjan, R., Kissel, R., Urbassek, H.M., 2000. Phys. Rev. B 62, 8487.
Colla, T.J., Urbassek, H.M., 2000. Nucl. Instrum. Meth. B 164–165, 687.
Conrad, U., Urbassek, H.M., 1990. Nucl. Instrum. Meth. B 48, 399.
Dingus, R.S., Scammon, R.J., 1991. SPIE Proc. Series 1427, 45.
Donnelly, S.E., Birtcher, R.C., 1997. Phys. Rev. B 56, 13599.
Eckstein, W., 1988. Nucl. Instrum. Meth. B 33, 489.
Eckstein, W., Biersack, J., 1984. Nucl. Instrum. Meth. B 2, 550.
Eckstein, W., Garcia-Rosales, C., Roth, J., Laszlo, J., 1993. Nucl. Instrum. Meth. B 83, 95.
Falcone, G., Sigmund, P., 1981. Appl. Phys. 25, 307.
Gades, H., Urbassek, H.M., 1992. Nucl. Instrum. Meth. B 69, 232.
Gades, H., Urbassek, H.M., 1994a. Phys. Rev. B 50, 11167.
Gades, H., Urbassek, H.M., 1994b. Nucl. Instrum. Meth. B 88, 218.
Garcia-Rosales, C., Eckstein, W., Roth, J., 1994. J. Nucl. Mater. 218, 8.
Georgiou, S., Hillenkamp, F. (Eds.), 2003. Thematic Issue: Laser Ablation of Molecular Substrates. Chem. Rev., vol. 103.
Gerhard, W., Oechsner, H., 1975. Z. Phys. B 22, 41.
Glazov, L.G., Shulga, V.I., Sigmund, P., 1998. Surf. Interface Anal. 26, 512.
Gnaser, H., 1999. Low-Energy Ion Irradiation of Solid Surfaces. Springer Tracts in Modern Physics, vol. 146. Springer, Berlin.
Graves, J.S., Allen, R.E., 1998. Phys. Rev. B 58, 13627.
Inogamov, N., 2006. Private communication.
Ivanov, D.S., Zhigilei, L.V., 2003. Phys. Rev. B 68, 064114.
Jeschke, H.O., Garcia, M.E., Bennemann, K.H., 2001. Phys. Rev. Lett. 87, 015002.
Johnson, R.E., 1990. Energetic Charged-Particle Interactions with Atmospheres and Surfaces. Springer, Berlin.
Johnson, R.E., 1994. Int. J. Mass Spectrom. Ion Proc. 139, 25.
Johnson, R.E., Evatt, R., 1980. Radiat. Eff. 52, 187.
Johnson, R.E., Schou, J., 1993. Mat. Fys. Medd. K. Dan. Vidensk. Selsk. 43, 403.
Johnson, R.E., Sundqvist, B.U.R., 1992. Phys. Today 45 (5), 28.
Johnson, R.E., Sundqvist, B.U.R., Hedin, A., Fenyö, D., 1989. Phys. Rev. B 40, 49.
Karolewski, M.A., 2006. Nucl. Instrum. Meth. B 243, 43.
Kelly, R., 1990. Nucl. Instrum. Meth. B 46, 441.
Kitazoe, Y., Hiraoka, N., Yamamura, Y., 1981. Surf. Sci. 111, 381.
Können, G.P., Tip, A., de Vries, A.E., 1974. Radiat. Eff. 21, 269.
Können, G.P., Tip, A., de Vries, A.E., 1975. Radiat. Eff. 26, 23.
Landau, L.D., Lifshits, E.M., 1960. Mechanics. Pergamon, New York.
Leveugle, E., Ivanov, D.S., Zhigilei, L.V., 2004. Appl. Phys. A 79, 1643.
Lindhard, J., Nielsen, V., Scharff, M., 1968. Mat. Fys. Medd. Dan. Vid. Selsk. 36 (10).
Lindhard, J., Scharff, M., 1961. Phys. Rev. 124, 128.
Littmark, U., Hofer, W.O., 1978. J. Mater. Sci. 13, 2577.
Michely, T., Comsa, G., 1991. Phys. Rev. B 44, 8411.
Michely, T., Krug, J., 2004. Islands, Mounds, and Atoms. Springer Series in Surface Science, vol. 42. Springer, Berlin.
Michely, T., Teichert, C., 1994. Phys. Rev. B 50, 11156.
Michl, J., 1983. Int. J. Mass Spectrom. Ion Phys. 53, 255.
Miotello, A., Kelly, R., 1997. Nucl. Instrum. Meth. B 122, 458.
Nastasi, M., Mayer, J.W., Hirvonen, J.K., 1996. Ion–Solid Interactions: Fundamentals and Applications. Cambridge University Press, Cambridge.
Nolte, S., Momma, C., Jacobs, H., Tünnermann, A., Chichkov, B.N., Wellegehausen, B., Welling, H., 1997. J. Opt. Soc. Am. B 14, 2716.
Nordlund, K., Henriksson, K.O.E., Keinonen, J., 2001. Appl. Phys. Lett. 79, 3624.
Nordlund, K., Tarus, J., Keinonen, J., Donnelly, S.E., Birtcher, R.C., 2003. Nucl. Instrum. Meth. B 206, 189.

Paltauf, G., Dyer, P.E., 2003. Chem. Rev. 103, 487.
Perez, D., Lewis, L.J., 2002. Phys. Rev. Lett. 89, 255504.
Perez, D., Lewis, L.J., 2003. Phys. Rev. B 67, 184102.
Phipps, C.R., Dreyfus, R.W., 1993. In: Vertes, A., Gijbels, R., Adams, F. (Eds.), Laser Ionization Mass Analysis. In: Chemical Analysis, vol. 124. Wiley, New York, p. 369.
Pines, D., Nozières, P., 1966. The Theory of Quantum Liquids, vol. 1. Normal Fermi Liquids. Benjamin, New York.
Preuss, S., Demchuk, A., Stuke, M., 1995. Appl. Phys. A 61, 33.
Rehn, L.E., Birtcher, R.C., Donnelly, S.E., Baldo, P.M., Funk, L., 2001. Phys. Rev. Lett. 87, 207601.
Reimann, C.T., 1993. Mat. Fys. Medd. K. Dan. Vidensk. Selsk. 43, 351.
Reimann, C.T., 1995. Nucl. Instrum. Meth. B 95, 181.
Rethfeld, B., Kaiser, A., Vicanek, M., Simon, G., 1999. Appl. Phys. A [Suppl.] 69, S109.
Rethfeld, B., Kaiser, A., Vicanek, M., Simon, G., 2002a. Phys. Rev. B 65, 214303.
Rethfeld, B., Sokolowski-Tinten, K., von der Linde, D., Anisimov, S.I., 2002b. Phys. Rev. B 65, 092103.
Samartsev, A.V., Duvenbeck, A., Wucher, A., 2005. Phys. Rev. B 72, 115417.
Schäfer, C., 2001. Molecular-dynamics of laser ablation of metals. Diploma thesis, University Kaiserslautern.
Schäfer, C., Urbassek, H.M., Zhigilei, L.V., 2002. Phys. Rev. B 66, 115404.
Schou, J., 2006. In: Pauleau, Y. (Ed.), Materials Surface Processing by Directed Energy Techniques. Elsevier. Chapter 2.
Seitz, F., Köhler, J.S., 1956. In: Seitz, F., Turnbull, D. (Eds.), Solid State Physics, vol. 2. Academic Press, Boston, p. 305.
Shulga, V.I., Eckstein, W., 1998. Nucl. Instrum. Meth. B 145, 492.
Sibold, D., Urbassek, H.M., 1993. J. Appl. Phys. 73, 8544.
Sigmund, P., 1969. Phys. Rev. 184, 383.
Sigmund, P., 1972. In: Kurepa, M.V. (Ed.), Physics of Ionized Gases. Institute of Physics, Beograd, Yugoslavia, p. 137.
Sigmund, P., 1974. Appl. Phys. Lett. 25, 169, 27 (1975) 52.
Sigmund, P., 1981. In: Behrisch, R. (Ed.), Sputtering by Particle Bombardment I. Springer, Berlin, p. 9.
Sigmund, P., 1987. Nucl. Instrum. Meth. B 27, 1.
Sigmund, P., Claussen, C., 1981. J. Appl. Phys. 52, 990.
Sigmund, P., Oliva, A., Falcone, G., 1982. Nucl. Instrum. Meth. 194, 541.
Slater, J.C., 1940. Phys. Rev. 57, 744.
Stampfli, P., Bennemann, K.H., 1990. Phys. Rev. B 42, 7163.
Staudt, C., Heinrich, R., Wucher, A., 2000. Nucl. Instrum. Meth. B 164–165, 677.
Süle, P., Menyhard, M., Nordlund, K., 2003. Nucl. Instrum. Meth. B 211, 524.
Thompson, M.W., 1968. Philos. Mag. 18, 377.
Urbassek, H.M., 1988. Nucl. Instrum. Meth. B 31, 541.
Urbassek, H.M., Hofer, W.O., 1993. Mat. Fys. Medd. K. Dan. Vidensk. Selsk. 43, 97.
Urbassek, H.M., Michl, J., 1987. Nucl. Instrum. Meth. B 22, 480.
Vicanek, M., Jimenez Rodriguez, J.J., Sigmund, P., 1989. Nucl. Instrum. Meth. B 36, 124.
Vidal, F., Johnston, T.W., Kieffer, J.-C., Martin, F., 2004. Phys. Rev. B 70, 184125.
Vogel, A., Venugopalan, V., 2003. Chem. Rev. 103, 577.
Wahl, M., Wucher, A., 1994. Nucl. Instrum. Meth. B 94, 36.
Waldeer, K.T., Urbassek, H.M., 1987. Nucl. Instrum. Meth. B 18, 518.
Waldeer, K.T., Urbassek, H.M., 1991. Physica A 176, 325.
Wang, X.Y., Riffe, D.M., Lee, Y.-S., Downer, M.C., 1994. Phys. Rev. B 50, 8016.
Weller, R.A., Weller, M.R., 1982. Nucl. Instrum. Meth. 194, 573.
Winterbon, K.B., Urbassek, H.M., Sigmund, P., Gras-Martí, A., 1987. Phys. Scripta 36, 689.
Wittmaack, K., 1997. Phys. Rev. B 56, R5701.
Wittmaack, K., 2003. Phys. Rev. B 68, 235211.
Wucher, A., Garrison, B.J., 1992a. Surf. Sci. 260, 257.
Wucher, A., Garrison, B.J., 1992b. Phys. Rev. B 46, 4855.
Ye, M., Grigoropoulos, C.P., 2001. J. Appl. Phys. 89, 5183.

Zel'dovich, Y.B., Raizer, Y.P., 1966. Physics of Shock Waves and High-Temperature Hydrodynamic Phenomena, vol. 1. Academic Press, New York.
Zhakhovskii, V.V., Nishihara, K., Anisimov, S.I., Inogamov, N.A., 2000. JETP Lett. 71, 167.
Zhigilei, L.V., Leveugle, E., Garrison, B.J., Yingling, Y.G., Zeifman, M.I., 2003. Chem. Rev. 103, 321.
Ziegler, J.F., 2000. Srim: http://www.srim.org/.
Ziegler, J.F., 2004. Nucl. Instrum. Meth. B 219–220, 1027.
Ziegler, J.F., Biersack, J.P., Littmark, U., 1985. The Stopping and Range of Ions in Solids. Pergamon, New York.